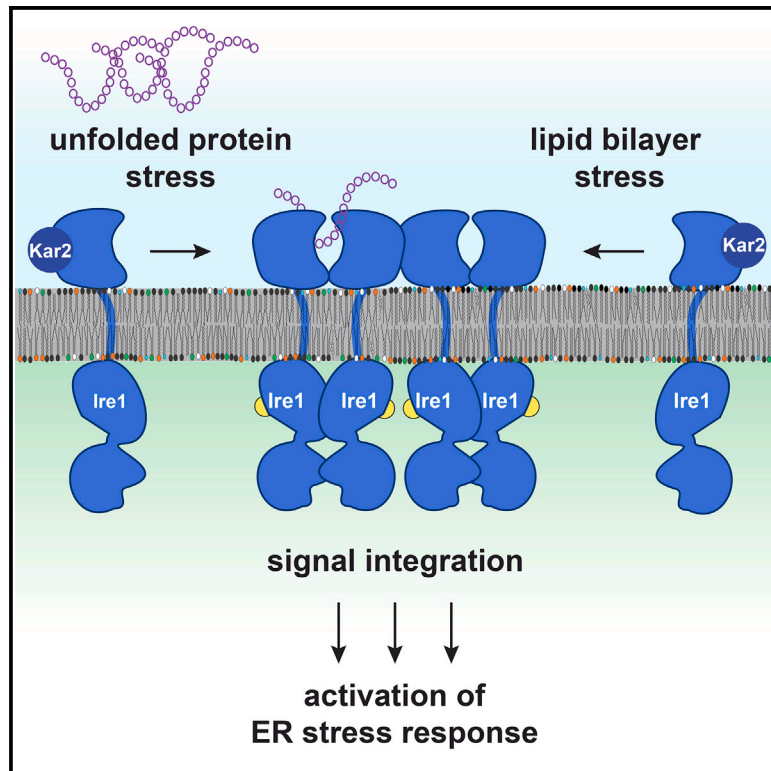# Molecular Cell

Activation of the Unfolded Protein Response by Lipid Bilayer Stress

Graphical Abstract

Authors

Kristina Halbleib, Kristina Pesek, Roberto Covino, ..., Inga Hänelt, Gerhard Hummer, Robert Ernst

Correspondence

robert.ernst@uks.eu

In Brief

The unfolded protein response (UPR) controls the secretory capacity of a cell and is activated by accumulating unfolded proteins in the lumen of the ER. More recently, it became obvious that aberrant membrane lipid compositions of the ER are equally potent in activating the UPR. Halbleib et al. identify a membrane-based mechanism of UPR activation and establish that Ire1, the most conserved transducer of ER stress, uses an amphipathic helix to sense and respond to aberrant physical properties of the ER membrane.

Highlights

- Aberrant lipid compositions of the ER activate the unfolded protein response

- Ire1 integrates two forms of ER stress: unfolded proteins and lipid bilayer stress

- Ire1 uses an amphipathic helix to sense aberrant physical membrane properties

- Local bilayer compression by Ire1 controls its membrane-sensitive activation

CellPress

Molecular Cell

Article

CellPress

Activation of the Unfolded Protein Response by Lipid Bilayer Stress

Kristina Halbleib,[1] Kristina Pesek,[1] Roberto Covino,[2] Harald F. Hofbauer,[1] Dorith Wunnicke,[3] Inga Hänelt,[3] Gerhard Hummer,[2,4] and Robert Ernst[1,5,6,*]

[1]Institute of Biochemistry and Buchmann Institute for Molecular Life Sciences, Goethe-University, Frankfurt, Max-von-Laue-Strasse 15, 60438 Frankfurt, Germany
[2]Department of Theoretical Biophysics, Max-Planck-Institute of Biophysics, Max-von-Laue-Strasse 3, 60438 Frankfurt, Germany
[3]Institute of Biochemistry, Goethe-University, Frankfurt, Max-von-Laue-Strasse 9, 60438 Frankfurt, Germany
[4]Institute of Biophysics, Goethe-University, 60438 Frankfurt, Germany
[5]Department of Medical Biochemistry and Molecular Biology, Saarland University, 66421 Homburg, Germany
[6]Lead Contact
*Correspondence: robert.ernst@uks.eu
http://dx.doi.org/10.1016/j.molcel.2017.06.012

SUMMARY

The unfolded protein response (UPR) is a conserved homeostatic program that is activated by misfolded proteins in the lumen of the endoplasmic reticulum (ER). Recently, it became evident that aberrant lipid compositions of the ER membrane, referred to as lipid bilayer stress, are equally potent in activating the UPR. The underlying molecular mechanism, however, remained unclear. We show that the most conserved transducer of ER stress, Ire1, uses an amphipathic helix (AH) to sense membrane aberrancies and control UPR activity. In vivo and in vitro experiments, together with molecular dynamics (MD) simulations, identify the physicochemical properties of the membrane environment that control Ire1 oligomerization. This work establishes the molecular mechanism of UPR activation by lipid bilayer stress.

INTRODUCTION

Secretory and transmembrane proteins of the secretory pathway are folded and assembled in the endoplasmic reticulum (ER) before they are distributed to their target destination via vesicular traffic. When the secretory load surpasses the folding capacity of the ER, misfolded proteins accumulate in the membrane and the lumen of the ER, a condition referred to as ER stress. The unfolded protein response (UPR) represents a program for cellular adaptation to ER stress involving a large-scale transcriptional response. The targets of the UPR include genes involved in protein folding, secretion, and degradation, as well as lipid biosynthesis (Cox et al., 1993; Jonikas et al., 2009; Travers et al., 2000; Walter and Ron, 2011).

The inositol-requiring enzyme 1 (Ire1) is the most conserved sensor of ER stress and crucial for UPR activation in yeast, plants, and metazoans (Cox et al., 1993; Kimata and Kohno, 2011; Mori, 2009; Mori et al., 1993; Tirasophon et al., 1998). It is embedded in the ER membrane via a single transmembrane helix (TMH) and senses unfolded proteins via its N-terminal sensor domain residing in the ER lumen (Figure 1A). The binding of unfolded proteins and the concomitant dissociation of the ER chaperone Kar2/BiP trigger the oligomerization of Ire1 (Gardner and Walter, 2011; Kimata et al., 2004, 2007). On the cytosolic side, Ire1 contains a kinase domain and an endoribonuclease (RNase) effector domain that are activated by oligomerization (Cox et al., 1993; Mori et al., 1993; Sidrauski and Walter, 1997). The regulated RNase activity of Ire1 initiates unconventional splicing of the *HAC1* mRNA precursor as a prerequisite for the production of the transcriptional activator Hac1 (Mori et al., 1996; Sidrauski and Walter, 1997). Hac1 is imported into the nucleus and binds to unfolded protein response elements (UPREs) to activate the expression of UPR target genes (Mori et al., 1996). The mammalian UPR is more complex than in baker's yeast and relies on the coordinated action of three major branches defined by the upstream transducers of ER stress: IRE1 (inositol requiring enzyme 1), PERK (double-stranded RNA-activated protein kinase [PKR]-like ER kinase), and ATF6 (activating transcription factor 6) (Walter and Ron, 2011). The UPR has been implicated in a number of pathological conditions including cancer, type II diabetes, and neurodegenerative diseases such as Alzheimer's (Fu et al., 2011; Özcan et al., 2004; Walter and Ron, 2011).

A classical way of studying the UPR is in the context of massive ER stress induced by the reducing agent dithiothreitol (DTT), which interferes with the formation of disulfide bridges in the lumen of the ER. It came as a surprise that the ΔIII mutant of Ire1, which cannot bind unfolded proteins, activates the UPR in DTT-stressed cells (Kimata et al., 2007; Promlek et al., 2011). The strength of activation was similar in mutant and WT cells, but significantly delayed for the mutant (Promlek et al., 2011). As this delayed response cannot be due to the binding of unfolded proteins, it was proposed to rely on changes of the ER lipid composition during prolonged periods of ER stress (Promlek et al., 2011). If so, DTT would activate the UPR both by interfering with protein folding in the ER
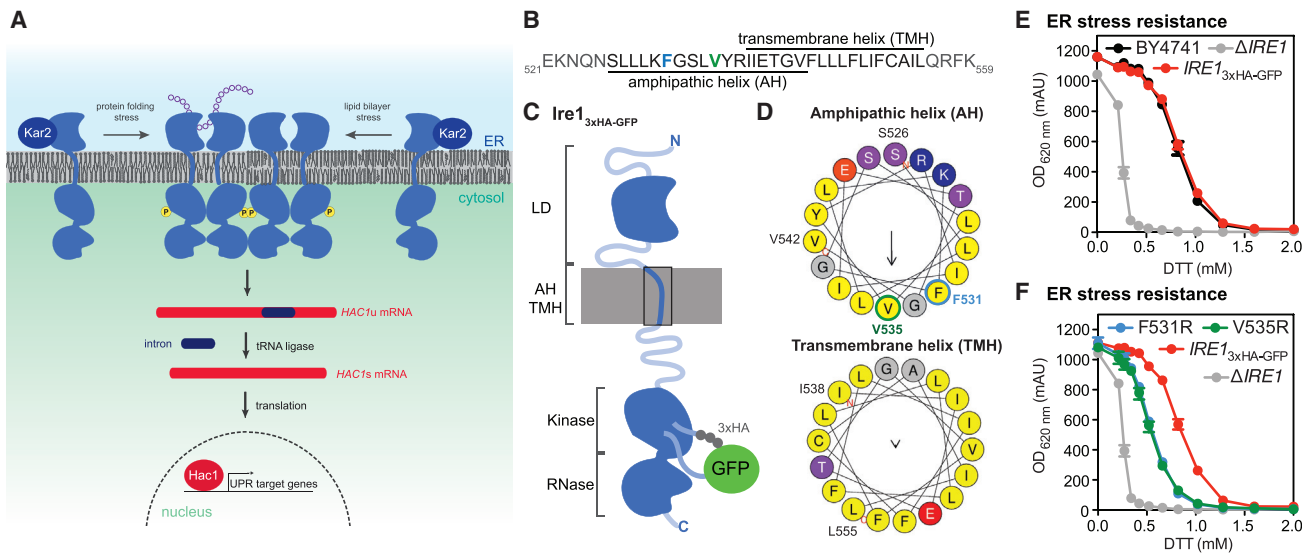
Figure 1. Ire1 Contains an AH Adjacent to the TMH on the ER-Lumenal Side Involved in UPR Activation

(A) The binding of unfolded proteins in the lumen of the ER induces Ire1 oligomerization and UPR activation. Lipid bilayer stress emerged as an additional activator of the UPR. The oligomerization of Ire1 is required for the activation of its cytosolic kinase and RNase domain. The RNase domain mediates the unconventional splicing of the *HAC1* mRNA in concert with the yeast tRNA ligase Rlg1. After translation of the spliced *HAC1* mRNA, the transcription factor Hac1 activates UPR target gene expression.

(B) The predicted TMH of Ire1 overlaps with a putative AH on the ER-lumenal side. Residues mutated in the course of this study are highlighted in blue (F531) and green (V535).

(C) Schematic representation of the Ire1 variant used in this study.

(D) HeliQuest analysis of the AH (Ire1$^{526-547}$) and the TMH (Ire1$^{538-555}$) of Ire1 (Gautier et al., 2008).

(E) Growth assay of the indicated yeast strains. Cells were cultivated in minimal medium (SCD) supplemented with the given concentrations of DTT at 30°C for 18 hr, and the density of the culture was determined using the OD$_{620}$.

(F) Growth assay of the indicated AH mutants as in (E).

The error bars represent the mean ± SEM of at least three independent experiments. See also Figures S1 and S2 and Tables S1 and S2.

and by inducing lipid bilayer stress. A much milder form of ER stress is induced by inositol depletion, which does not result in a detectable accumulation of unfolded proteins in the lumen of the ER (Lajoie et al., 2012; Merksamer et al., 2008). Instead, it seems to activate the UPR entirely by a membrane-based mechanism and independently of unfolded proteins (Promlek et al., 2011). These findings suggested that Ire1 might sense two fundamentally distinct types of signals: unfolded proteins and lipid bilayer stress. Similar observations for the mammalian transducers of ER stress IRE1α and PERK point in the same direction and suggest that membrane responsiveness might be a conserved feature of the UPR (Volmer et al., 2013). Even in the absence of an ER-lumenal domain, which is required for binding of unfolded proteins, IRE1α and PERK are activated by aberrant membrane environments (Volmer et al., 2013). It was shown that membrane tethering by the TMH is crucial for membrane-responsiveness of IRE1α and PERK, but the structural element(s) and mechanism(s) rendering these proteins particularly sensitive to aberrant lipid compositions remained elusive (Volmer et al., 2013). Given the broad and fundamental importance of the UPR in cellular physiology, these findings provided a fresh perspective on the role of lipids in health and disease (Walter and Ron, 2011). Here, we describe the mechanism of UPR activation by lipid bilayer stress.

RESULTS

Ire1 Contains a Conserved Amphipathic Helix Important for Function

How does Ire1 sense diverse aberrant ER lipid compositions caused by dysregulated sphingolipid production (Han et al., 2010), disrupted sterol homeostasis (Pineau et al., 2009), inositol depletion (Lajoie et al., 2012; Promlek et al., 2011), impaired phosphatidylcholine (PC) biosynthesis (Thibault et al., 2012), and increased proportions of saturated membrane lipids (Pineau et al., 2009; Surma et al., 2013; Volmer et al., 2013)? We approached this question by a systematic inspection of the transmembrane helix (TMH) region of the baker's yeast Ire1 revealing a putative amphipathic helix (AH) (Ire1$^{526-543}$) adjacent to and overlapping with the ER-lumenal end of the TMH (Ire1$^{538-555}$) (Figures 1B–1D) (Gautier et al., 2008). The predicted AH exhibits a large hydrophobic face composed of aromatic and hydrophobic residues and a small hydrophilic face composed of polar and charged residues (Figure 1D). Intriguingly, the amphipathic character of the ER-lumenal, juxta-membrane region is conserved in Ire1 among eukaryotes including mammals, plants, and numerous fungi as well as in the mammalian PERK (Figures S1A and S1B). CD spectroscopy revealed that a synthetic peptide (Ire1$^{522-543}$) of the predicted AH is unstructured in aqueous buffer, but acquires an α-helical fold in the presence of a hydrophobic

matrix provided by detergent micelles of n-Dodecyl-β-D-maltoside (Figure S2A), thereby revealing the potential to form an AH.

To test the physiological relevance of the juxta-membrane AH, we generated a knock-in construct for the expression of *IRE1* from its endogenous genomic locus and promoter. For detection, Ire1 was internally tagged with GFP and a 3xHA epitope tag inserted in a flexible loop at the position H875 (van Anken et al., 2014) (Figure 1C; Tables S1 and S2). Compared to an expression strategy based on *CEN*-based plasmids, our knock-in approach provided a >2.5-fold lower steady-state level of this low-abundance signaling protein (Figure S2B) and seemed to accomplish a lower cell-to-cell heterogeneity of expression (Figure S2C). Due to its low copy number, Ire1$_{3xHA-GFP}$ cannot be detected in unstressed knock-in cells above the autofluorescence background (Figure S2D). Nevertheless, cells producing the internally tagged variant were phenotypically indistinguishable from isogenic wild-type (BY4741) cells, while cells lacking *IRE1* were highly sensitive to long-term ER stress induced by DTT (Figure 1E). Thus, the functionality of the engineered knock-in construct was confirmed by a sensitive phenotypic readout.

Previous studies on the mammalian IRE1α have suggested a critical role of the TMH for membrane responsiveness (Volmer et al., 2013). However, upon scrambling or substitution of the TMH by an unrelated ER membrane protein, the resulting molecule remained responsive to the membrane environment (Volmer et al., 2013). This suggested that the TMH does not contain a specific structural feature that would contribute to the activation of the UPR in response to lipid bilayer stress (Volmer et al., 2013). In light of these observations, we tested the role of Ire1's TMH and AH for normal function. We exchanged either 13 (L13; Ire1$^{543-555}$) or 16 (L16; Ire1$^{540-555}$) residues of the TMH with a poly-leucine stretch (Figure S2E). Both variants were properly inserted into the ER membrane (Figure S2F). Even though the substitution of 13 TMH residues would remove potentially important sequence elements from the TMH, it did not impose any functional defect as validated by our sensitive growth assay (Figure S2G). However, the substitution of three additional residues from the N-terminal end of the TMH overlapping with the predicted AH region (L16) resulted in a significantly decreased cellular resistance to DTT (Figure S2H). These observations suggested an important role of the AH region for normal Ire1 function.

In order to validate this interpretation, we disrupted the amphipathic character of the AH by substituting either F531 or V535 to arginine (Figure 1D). WT *IRE1* and both mutant variants were expressed to a comparable level in unstressed and stressed cells (Figures S2I and S2J) and were properly integrated in the ER membrane (Figure S2K). Nevertheless, when the AH was disrupted either by the F531R or the V535R mutation, the cellular resistance to DTT was markedly reduced (Figure 1F). Remarkably, a mutation on the hydrophilic side of the AH (R537E), which changes the local charge but not the amphipathic character of the helix, did not impose any detectable functional defect (Figure S2L). Together, these observations underscore the importance of the AH for Ire1's normal function.

Because UPR activation relies on a local confinement of oligomeric Ire1 (van Anken et al., 2014; Aragón et al., 2009), we imaged acutely stressed cells by confocal fluorescence microscopy. We aimed at studying the clustering of Ire1 during the onset of the UPR and imaged cells that were acutely stressed by DTT (1.5 hr, 10 mM DTT, SCD). Due to the low copy number of Ire1$_{3xHA-GFP}$ and the relatively high background fluorescence of *S. cerevisiae*, it was not possible to localize Ire1$_{3xHA-GFP}$ in unstressed cells (Figure S2D). In stressed cells, however, clusters of Ire1$_{3xHA-GFP}$ could be observed as punctate structures with high fluorescence intensity (Figure 2A) that were more prevalent in cells overproducing Ire1$_{3xHA-GFP}$ (Figure S2C). The abundance of Ire1$_{3xHA-GFP}$ containing clusters was significantly reduced in cells expressing the F531R or the V535R mutant (Figure 2A). Inositol depletion represents a milder form of ER stress that establishes over a longer period of time (3 hr) and results in UPR activation without triggering massive protein unfolding (Lajoie et al., 2012; Merksamer et al., 2008; Promlek et al., 2011). Consistently, WT Ire1$_{3xHA-GFP}$ formed smaller clusters of lower intensity that were barely distinguishable from the autofluorescence background under this condition (Figure 2A). Still, the formation of these low-intensity clusters was significantly impaired by the F531R and the V535R mutation (Figure 2A). Together, these data suggest that the increased sensitivity of cells producing Ire1$_{3xHA-GFP}$ with a disrupted juxta-membrane AH is due to a defect in the oligomerization and activation of Ire1.

We then tested the degree of *HAC1* mRNA splicing in unstressed and stressed cells. Consistent with the observations from microscopy, the unconventional splicing of the *HAC1* mRNA in response to an acute (1 hr) and harsh ER stress in rich medium (4 mM DTT) was markedly impaired for the V535R variant compared to the WT (Figure 2B), revealing that a disrupted AH also impairs Ire1 activation. Similarly, the response to inositol depletion was significantly impaired for the mutant (Figure 2B). The mRNA level of the UPR-target gene *PDI1* increased in Ire1$_{3xHA-GFP}$ WT producing cells >5-fold and >2.5-fold during ER stress induced by DTT and depletion of inositol, respectively (Figure 2C). In contrast, mutant cells producing the AH-disrupted Ire1$_{3xHA-GFP}$ V535R variant barely upregulated the mRNA of *PDI1* in response to ER stress (Figure 2C). Taken together, we identified functional defects for the AH-disrupted mutants in the context of two types of ER stress under conditions of acute and long-term challenges and upon cultivation of cells in both rich and minimal medium. Collectively, our data highlight a crucial importance of Ire1's AH in UPR activation.

Ire1 is a protein with many biochemical functions, which rely on molecular interactions with the post-translational protein translocation apparatus of the ER and the ER-lumenal chaperone Kar2/BiP (Kimata et al., 2004; Pincus et al., 2010; Plumb et al., 2015). We performed co-immunoprecipitation (IP) experiments with Ire1, Sec63 as a component of the post-translational protein translocation apparatus, and endogenous Kar2/BiP to test if the V535R and F531R mutations interfere with these interactions in both the absence and the presence of ER stress. When we immunoisolated Sec63 via a C-terminal 3xFlag-tag (Figure 2D), we co-precipitated Ire1 WT and the F531R and V535R variants with comparable efficacy (Figure 2D). Thus, the AH-disrupting mutations do not interfere with the formation of a complex between Sec63 and Ire1 in both stressed and unstressed cells. Similarly, when Ire1 WT and its mutant F531R and V535R

CellPress
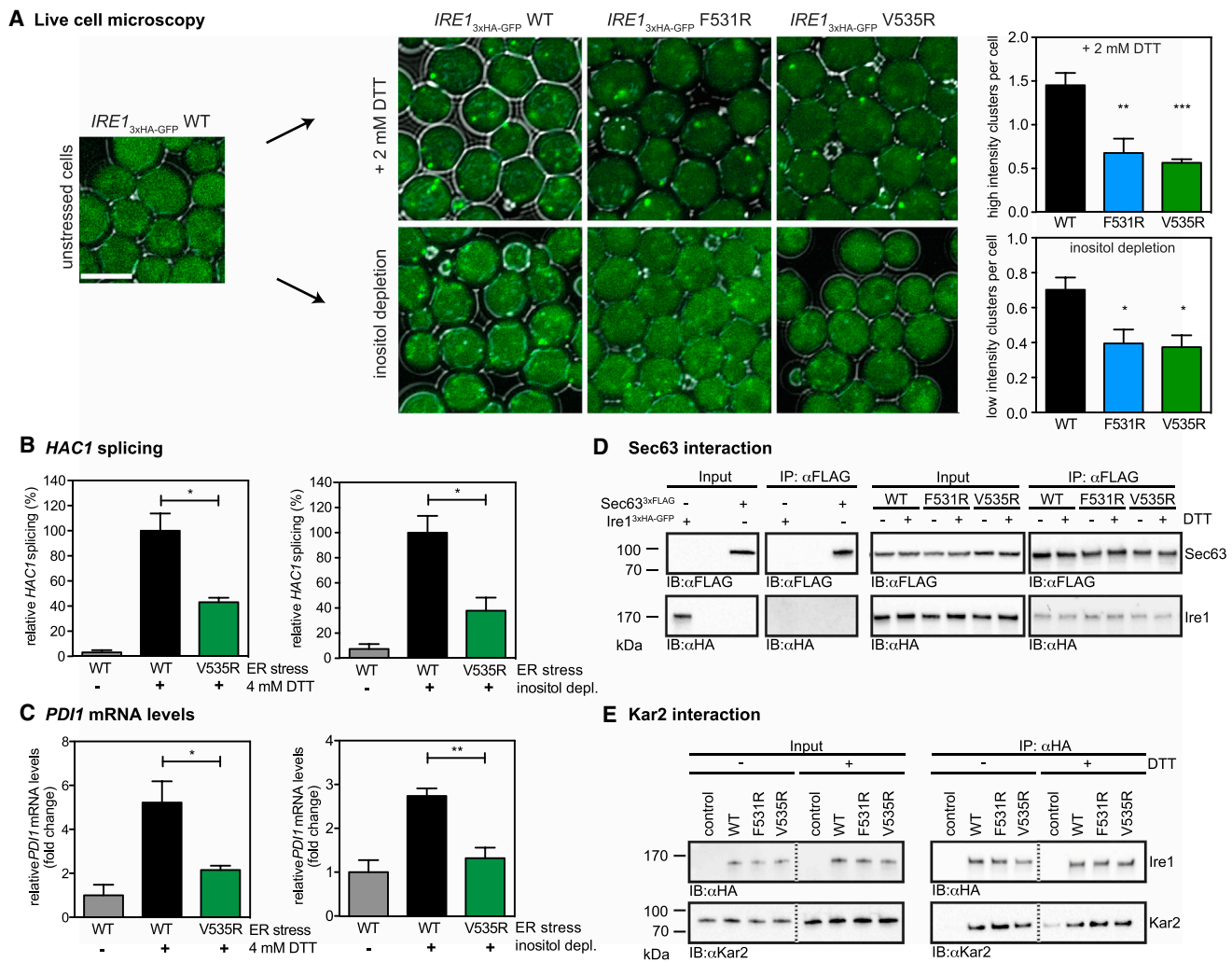
Figure 2. Mutations in the AH Affect the Functionality of Ire1

(A) Live cell confocal microscopy of indicated yeast strains during acute ER stress. Cells were treated with DTT (1.5 hr, 10 mM DTT, SCD) or cultured in inositol depleted medium (3 hr). Quantification of high and low intensity clusters of Ire1 based on a semi-automated script. The error bars represent the mean ± SEM from three independent experiments with a minimum of 40 cells from randomly chosen fields of view being analyzed for each replicate. Scale bar, 5 μm.

(B and C) Levels of spliced *HAC1* mRNA (B) and *PDI1* mRNA (C). The indicated knock-in strains were stressed by a treatment with DTT (1 hr, 4 mM, YPD) or inositol depletion (3 hr), respectively, and analyzed by qRT-PCR. The degree of splicing, i.e., the fraction of spliced *HAC1* mRNA relative to the total *HAC1* mRNA, was roughly 63% in DTT-stressed WT cells and 46% in inositol-depleted cells as determined in independent experiments. For better visualization, the data were normalized in (B) to the degree of *HAC1* mRNA splicing in stressed WT cells and in (C) to the steady-state level of the *PDI1* mRNA in unstressed cells.

(D) Cells co-expressing either *SEC63*₃ₓFₗₐg, the *IRE1*₃ₓHA-GFP knock-in, or both constructs were lysed prior to an IP using anti-Flag beads. Co-immunoprecipitated Ire1₃ₓHA-GFP was detected by immunoblotting using anti-HA antibodies. The strain expressing only the *IRE1*₃ₓHA-GFP knock-in serves as a specificity control of the co-IP.

(E) Cells expressing *IRE1*₃ₓHA-GFP were lysed prior to an IP using anti-HA beads. Co-immunoprecipitated, endogenous Kar2/BiP was detected by immunoblotting using anti-Kar2 antibodies. The isogenic wild-type strain BY4741 that does not express a HA-tagged variant of *IRE1* was used as a specificity control (control). When indicated, cells were treated with DTT (1 hr, 10 mM, YPD), thereby increasing the endogenous level of Kar2/BiP.

All graphs show means ± SEM for at least three independent experiments, and statistical significance was tested by an unpaired, two-tailed Student's t test. ***$p < 0.001$, **$p < 0.01$, *$p < 0.05$.

variants were immunoisolated from cells, comparable levels of Kar2/BiP were co-precipitated from unstressed and stressed cells (characterized by a higher steady-state level of Kar2/BiP) (Figure 2E). Thus, AH-disrupting mutations do not impair the interactions between Ire1, Sec63, and Kar2/BiP, thereby suggesting that the functional defects observed for Ire1 with a disrupted

AH do not result from a perturbed interaction with modulatory interaction partners.

The oligomerization of Ire1 during ER stress occurs via specific ER-lumenal interfaces and is crucial for UPR activation (Credle et al., 2005). The ER-lumenal interface-1 (IF1) is required for the dimerization of Ire1, while interface-2 (IF2) mediates the
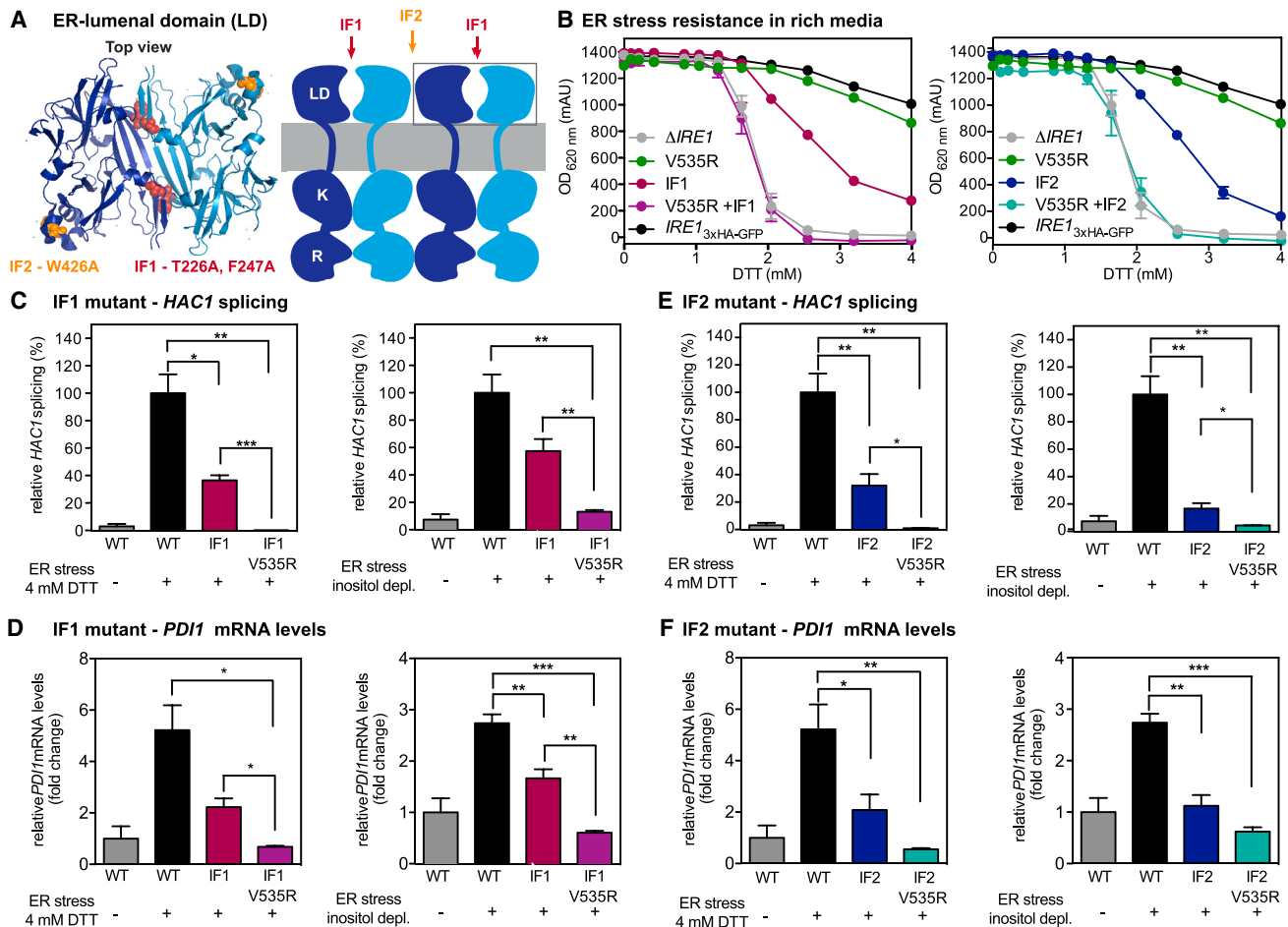
Figure 3. Negative Epistasis between Mutations in the AH and ER-Lumenal Interfaces
(A) Model of the dimeric ER-lumenal domain (LD) of Ire1 based on the X-ray structure (PDB: 2BE1) (Credle et al., 2005) in a top view representation and a schematic illustration of Ire1. Key residues contributing to IF1 (red) and IF2 (orange) and mutations interfering with Ire1 oligomerization are highlighted.
(B) Growth assay of the indicated yeast strains carrying mutations in IF1, IF2, and/or the AH region of Ire1. Cells were cultivated in rich medium and challenged with the given concentrations of DTT. Cellular growth was determined using the OD_{620}. The error bars represent the mean ± SEM of at least three independent experiments.
(C) The relative degree of *HAC1* mRNA splicing was determined by qRT-PCR for stressed and unstressed cell.
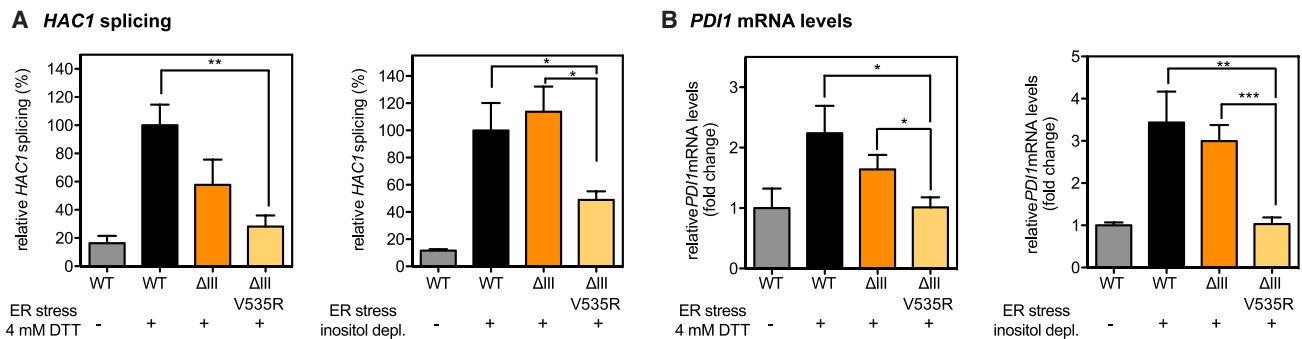(D) The relative level of the *PDI1* mRNA was determined by qRT-PCR for stressed and unstressed cells.
(E) The relative degree of *HAC1* mRNA splicing was determined by qRT-PCR for stressed and unstressed cells.
(F) The relative level of *PDI1* mRNA was determined by qRT-PCR for stressed and unstressed cells.
(C–F) The indicated cells were stressed by a treatment with DTT (1 hr, 4 mM, YPD media) or inositol depletion (3 hr), respectively.
The data were normalized as in Figures 2B and 2C. The error bars represent the average ± SEM of at least three independent experiments. Significance was tested by an unpaired, two-tailed Student's t test. ***$p < 0.001$, **$p < 0.01$, *$p < 0.05$.

interaction between dimers (Figure 3A). Consistent with previous findings (Credle et al., 2005), mutations in IF1 (T226A, F247A) and IF2 (W426A) impair UPR activity, as revealed by the cellular resistance to DTT (Figure 3B), quantification of the degree of *HAC1* splicing (Figure 3C), and UPR-target gene *PDI1* induction (Figure 3D). Intriguingly, much higher concentrations of DTT were required to block cellular growth in rich media compared to minimal media (Figures 1F and 3B). Whether this reflects a difference in the effective intracellular concentration of DTT or an increased cellular resistance to ER stress of cells cultivated in rich medium remains to be established. An AH-disrupting mutation in Ire1 (V535R) that significantly lowered the cellular

resistance to DTT in minimal media (Figure 1F) did not do so in rich media (Figure 3B). This was surprising because the activity of this mutant was clearly compromised during acute ER stress and even in rich medium (Figures 2B and 2C). Consistent with previous observations (Thibault et al., 2012), we speculate that adaptive responses of both the proteostasis and the lipid metabolic network become more relevant during prolonged periods of ER stress and particularly in minimal medium. Most strikingly, when the V535R mutation was combined with mutations in IF1 or IF2, the resulting cells exhibited a dramatically increased sensitivity to DTT, a phenotype comparable to an *IRE1* deletion strain (Figure 3B). We further characterized the ability of these

Figure 4. Binding of Unfolded Proteins and the AH of Ire1 Jointly Contribute to UPR Activation during ER Stress

(A and B) The relative degree of *HAC1* mRNA splicing (A) and the relative level of the *PDI1* mRNA (B) were determined for the indicated stressed and unstressed cells by qRT-PCR. The indicated cells were stressed by a treatment with DTT (30 min, 4 mM, YPD media) or inositol depletion (3 hr), respectively.

The data were normalized as in Figures 2B and 2C. The error bars represent the average ± SEM of at least three independent experiments. Significance was tested by an unpaired, two-tailed Student's t test. ***p < 0.001, **p < 0.01, *p < 0.05.

mutants to mediate splicing of the *HAC1* mRNA and to induce *PDI1* in response to two types of ER stress. Again, the combined IF1/V535R and IF2/V535R mutations, respectively, rendered the cells unresponsive to ER stress (Figures 3C–3F). These data identify a strong negative epistasis between these mutations and suggest that IF1, IF2, and the juxta-membrane AH jointly contribute to the oligomerization and activation of Ire1 in an additive fashion.

In order to uncouple the signals contributing to the activation of the UPR, we used the ΔIII mutant of Ire1, which cannot bind unfolded proteins (Kimata et al., 2007; Promlek et al., 2011), and combined it with the AH-disrupting mutation V535R. Consistent with previous findings (Kimata et al., 2007), the ΔIII mutant exhibited a defective response to acute ER stress induced by DTT but remained fully responsive to inositol depletion (Figures 4A and 4B). Thus, inositol depletion seems to activate the UPR independently of unfolded proteins, while DTT induces both protein unfolding and lipid bilayer stress. When the ΔIII and the V535R mutation were combined, the resulting cells failed to activate the UPR irrespectively of the ER stress-inducing condition (Figures 4A and 4B). The synthetic defects of the ΔIII and the AH-disrupting mutations were also reflected by the cellular resistance to DTT: while the ΔIII mutation had no effect on ER stress resistance (Figure S2M), the combined ΔIII/V535R mutation resulted in a loss-of-function phenotype and a cellular sensitivity comparable to *IRE1* knockout cells (Figure S2M). These data suggest that the binding of unfolded proteins is not the only signal contributing to the activation of Ire1 and establish a crucial role of its AH for UPR activation.
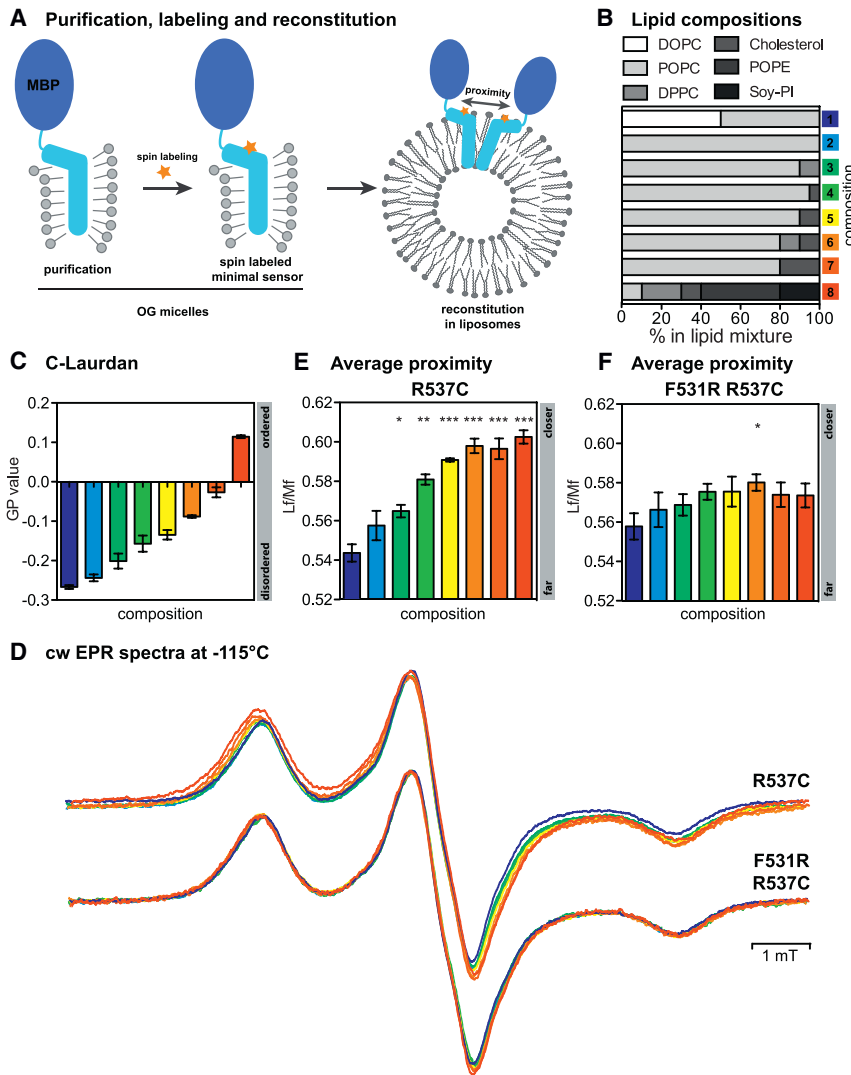
Reconstitution of a Minimal Sensor Construct in Defined Membrane Environments

We hypothesized that the unusual architecture of Ire1's TMH region containing a juxta-membrane AH overlapping with the TMH represents an important structural feature for sensing perturbed lipid compositions of the ER membrane. To test this hypothesis in vitro, we generated a minimal sensor construct comprised of the AH and the TMH (Ire1[526–561]) that was C-terminally fused to the maltose-binding protein. This minimal sensor was isolated

in the presence of octyl-β-D-glucopyranoside (OG) (Figures S3A and S3B) and successfully reconstituted in liposomes with defined lipid compositions (Figures 5A–5C and S3C–S3G). The average size of the liposomes was measured using the NanoSight technology and identical within the range of error for all lipid compositions. The lipid compositions 1–7 were chosen to form a uniform liquid-disordered membrane phase, while covering a wide range of molecular lipid packing densities and maintaining minimal complexity in the lipid headgroup region (Figure 5B). These lipid compositions were based entirely on a phosphatidylcholine (PC) matrix and differed only in their cholesterol content and the proportion of saturated lipid acyl chains. The lipid composition 8 was more complex (Figure 5B) and combined several characteristic lipidome changes observed in cells undergoing lipid bilayer stress: an increased degree of lipid saturation, an increased sterol level, and an increased PE:PC ratio (Pineau et al., 2009; Surma et al., 2013; Thibault et al., 2012). Instead of ergosterol, which is the most abundant sterol in *S. cerevisiae*, we used cholesterol in these experiments, as it bears similar physicochemical properties to ergosterol but is much better characterized (Klose et al., 2010). We determined the molecular lipid packing densities of the liposomes using the fluorescent reporter C-Laurdan (Figure 5C) and found that they covered the full range of generalized polarization (GP) values reported for organelles of the secretory pathway including the unstressed ER (GP value of −0.19 reported for dog pancreas microsomes) (Kaiser et al., 2011) and the trans-Golgi network (GP value of ∼0.09) (Klemm et al., 2009).

Membrane-Sensitive Oligomerization of the Minimal Sensor

If the unusual architecture of the TMH region is sufficient for the membrane-sensitive oligomerization and activation of Ire1, the minimal sensor should recapitulate this behavior. We thus characterized the oligomerization of the reconstituted minimal sensor using continuous-wave electron paramagnetic resonance (cwEPR) spectroscopy at −115°C allowing for detection of small inter-spin distances. Single-cysteine variants of the minimal sensor were generated and labeled with methanethiosulfonate (MTS)

Figure 5. cwEPR Spectroscopy Reveals Membrane-Sensitive Oligomerization of a Minimal Sensor Based on Ire1's AH and TMH

(A) Systematic representation of the in vitro purification, labeling, and reconstitution strategy.

(B) The minimal sensor domain was reconstituted in liposomes of indicated lipid compositions.

(C) C-Laurdan spectroscopic measurements determine the lipid packing of liposomes with indicated compositions. Lipid packing is represented as generalized polarization (GP) ranging from +1 (most ordered) to −1 (most disordered) membrane lipids.

(D) cwEPR spectra recorded at −115°C were intensity normalized and plotted using the color code for lipid compositions from (B).

(E and F) Semiquantitative analysis of inter-spin distances of the minimal sensor labelled at R537C (E) and the minimal sensor with a disrupted AH (F531R) labelled at R537C. The proximity index Lf/Mf was derived from spectra presented in (D) and plotted for the indicated lipid compositions with the color code from (B). Higher values indicate lower average inter-spin distances.

The error bars represent the average ± SEM for three independent experiments. Significance was tested by an unpaired Student's t test. ***p < 0.001, **p < 0.01, *p < 0.05. See also Figures S3, S4, and S6.

spin probes. Broadening of cwEPR spectra occurs only when the distal separation of two spin probes is less than ~1.8 nm, i.e., when the spin-labeled minimal sensor forms oligomers (Covino et al., 2016). Detailed line-shape analysis of the low (Lf) and middle (Mf) field peak allows for calculation of the Lf/Mf ratio as semiquantitative index for the distal separation of the spin labels (Figure S4A). The MTS spin probe was installed on the hydrophilic side of the AH at the position R537 of the minimal sensor (R537C), because this residue can be mutated without imposing functional defects in vivo (Figure S2L). We observed spectral broadening for the spin-labeled minimal sensor, which correlated with the molecular lipid packing: the more ordered the membrane environment, the more distinct the spectral broadening (Figures 5C–5E). Similar results were obtained when the spin probe was installed in the TMH of Ire1 at the position of the endogenous C552 (Figures S4B–S4D). Spin-diluted control spectra verified that spectral broadening was not due to unspecific effects of the membrane environment on the spin probe (Figures S4E–S4G). Thus, the minimal sensor oligomerizes in a membrane-sensitive fashion. The striking dependence of spectral broadening on the

molecular lipid packing densities suggests that a collective membrane property contributes to the oligomerization and activation of Ire1. When the juxta-membrane AH of the minimal sensor was disrupted by the F531R mutation, the membrane-sensitive oligomerization of the construct was greatly impaired, irrespective of the 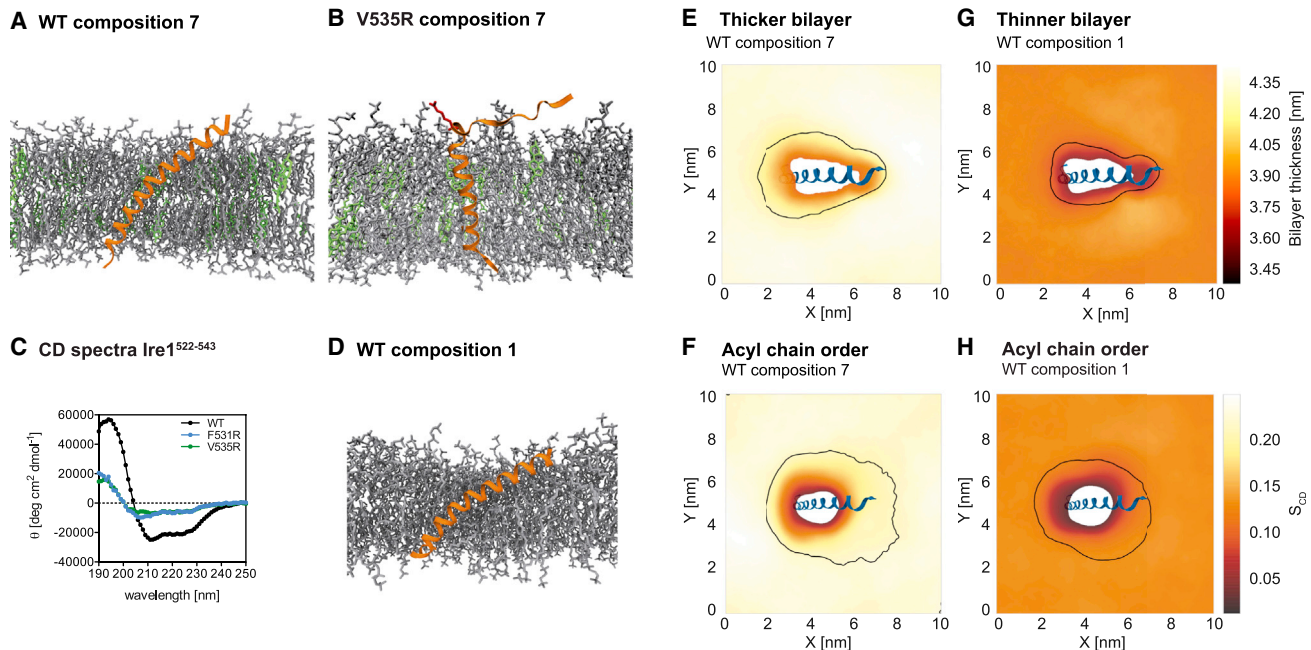position of spin labeling (Figures 5D, 5F, and S4C). This suggests that Ire1 uses its AH to sense lipid bilayer stress. Based on these findings, we propose that the multitude of functional defects observed for the AH-disrupted mutants in vivo (Figures 1, 2, 3, and 4) are due to an impaired response to aberrant ER membrane lipid compositions.

MD Simulations Reveal a Membrane-Based Activation Mechanism of Ire1

To gain insights into the dynamic properties of the juxtamembrane AH, we performed extensive atomistic molecular dynamics (MD) simulations of the sensor peptide comprised of the AH and the TMH (Ire1[526–561]), and of the two mutant variants V535R and F531R (Table S3). Sensor peptides were modeled as straight alpha helices (Figures S5A–S5C) and placed into lipid bilayers corresponding to the tightly packed lipid composition 7 (Figure 5C) of the in vitro reconstitution experiments. Within 100 ns of simulation, the WT helix underwent a considerable conformational change (Figure 6A; Movie S1). The hydrophobic portion of the AH entered the lipid bilayer and remained stably inserted throughout the >3 μs simulation, with the hydrophilic portion of the AH facing the aqueous environment. Intriguingly,

Figure 6. Mechanism of Ire1 Activation by Lipid Bilayer Stress

(A) Representative structure of the Ire1-derived sensor peptide (Ire1[526–561]) in a lipid bilayer (composition 7; Figure 5B), derived from an all-atom MD simulation and represented as an orange ribbon. The AH (Ire1[526–543]) remained stably inserted in the upper monolayer (corresponding to the ER-lumenal side) during the entire atomistic MD run of >3 μs (glycerophospholipids, gray; cholesterol, green; water, ions not shown).

(B) Representative structure of the V535R (red) variant of the sensor peptide from MD simulations. The AH rapidly unfolds and progressively disrupts over ~1.8 μs of the MD run and remains unfolded outside the bilayer.

(C) CD spectroscopic analysis of the indicated, synthetic AH peptides (Ire1[522–543]) in a sodium carbonate buffer (pH 7.0) supplemented with 1% DDM.

(D) Representative structure of the sensor peptide simulated in a loosely packed lipid bilayer (composition 1; Figure 5B), represented as in (A).

(E and G) Membrane thickness around the sensor peptide, defined as the average vertical distance between the two phosphate layers, averaged over MD simulations in bilayers of composition 7 (E) and composition 1 (G). The black solid contour line shows a 3% drop of the bilayer thickness from the bulk average. A representative structure of the peptide is shown, with the N terminus on the right lying on the ER-lumenal leaflet of the bilayer.

(F and H) The acyl chain order parameter S_{CD} reports on the orientational mobility of the C-D bond in the lipid tails. Profiles of S_{CD} were calculated around the sensor peptide and averaged over MD simulations in bilayers of composition 7 (F) and composition 1 (H). In averaging over the whole simulation time (E–H), the TMH region was aligned to a common reference by using rigid body translations and restricted rigid-body rotations around an axis normal to the membrane plane. The black contour line indicates a drop in S_{CD} by 3.5% relative to the average bulk value (estimated distant from the peptide).

See also Figure S5, Movies S1 and S2, as well as Table S3.

membrane integration of the AH forced the TMH into a highly tilted orientation relative to the normal of the lipid bilayer and induced transient kinking of the sensor peptide. The MD simulations of the V535R and F531R mutant variants of the sensor peptide revealed the crucial role of the AH for this unusual architecture (Figure 6B; Movie S2; Figures S5C and S5D). The AH region of these mutants unfolded within <1 μs and failed to insert into the lipid bilayer. As a consequence, the TMH of the mutant sensor peptide neither kinked nor tilted to the same extent as the WT variant. Thus, these MD simulations strongly suggest that the F531R and V535R mutations interfere with the architecture of Ire1's TMH region by disrupting both the amphipathic character and the helical fold of the AH. This interpretation is supported by CD spectra of synthetic peptides corresponding to the AH of Ire1[522–543] recorded in the presence of detergent micelles, showing significant unfolding of F531R and V535R peptides compared to the WT variant (Figure 6C).

To explore the effect of the membrane lipid composition, we performed additional MD simulations with the WT sensor peptide in a more loosely packed membrane environment corresponding to lipid composition 1 of the in vitro experiments (Figures 6D and S5E). Again, we observed an unusual, highly tilted conformation of the peptide similar to that observed in the more tightly packed lipid environment 7. This argues against a major structural change such as unfolding of the AH region in response to lipid bilayer stress. We validated this finding in vitro by recording low temperature cwEPR spectra of the isolated and reconstituted minimal sensor that was spin labeled individually at six consecutive residues in the AH region (Ire1[534–539]). The polarity of the spin probe's environment, referred to as the 2Azz value, was extracted from the spectra as the peak distance between the low and the high field peak (Figure S6A) (Bordignon and Steinhoff, 2007). When the polarity of the spin probes' environment was plotted against the position of labeling, a clear helical pattern of polarity could be observed in two lipid environments differing substantially in the molecular packing density (Figures S6B and S6C). This suggests that the AH is stably inserted into the lipid bilayer even in tightly packed
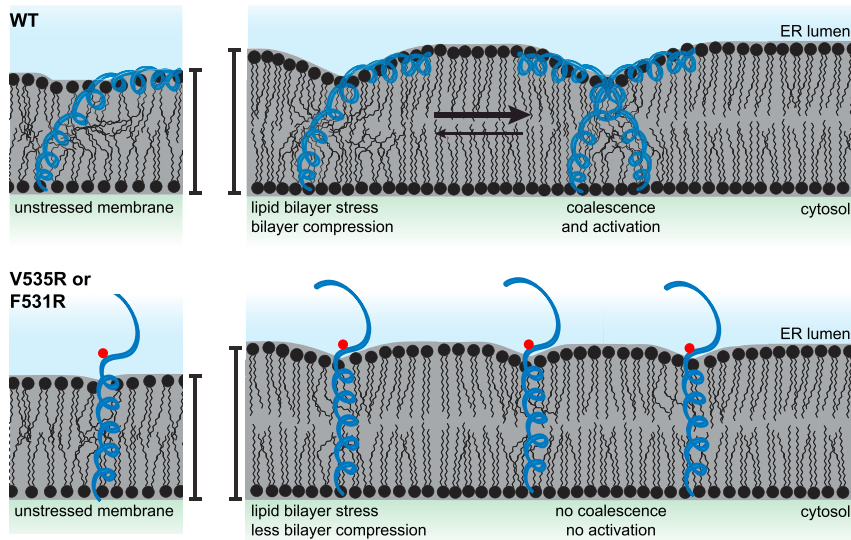
Figure 7. Schematic Model of the Membrane-Based Activation Mechanism of Ire1

The juxta-membrane AH on the ER-lumenal side of Ire1 WT (top) causes a local membrane compression. The total area of membrane compression is minimized upon oligomerization of Ire1. If the amphipathic character of the AH is disrupted by mutation (red), the corresponding residues fail to insert into the lipid bilayer and thus cause substantially less membrane compression.

membranes. The spectral broadening that was observed when the minimal sensor was labeled at the positions Y536C-I539C and reconstituted in a more densely packed membrane environment further corroborated our previous interpretation of a membrane-sensitive oligomerization of the minimal sensor (Figures S6B and S6D). No spectral broadening was observed, however, when the spin probe was installed at the more N-terminal positions L534C and V535C (Figures S6B and S6D), suggesting inter-spin distances greater than ~1.8 nm at these positions in the N-terminal part of the AH. Together, MD simulations and EPR spectroscopy data argue against a major impact of the lipid environment on the monomeric structure of Ire1. So if this is the case, how does the membrane environment affect the oligomerization of Ire1?

To explore how the membrane environment could affect Ire1 oligomerization, we revisited our MD simulations of the sensor peptide (Ire1$^{526-561}$) in two distinct membranes differing in their degree of molecular lipid packing. Composition 7, with its higher proportion of saturated lipid acyl chains and sterols, generally produces a thicker (Figure 6E) and more ordered (Figure 6F) lipid bilayer compared to composition 1 (Figures 6G and 6H). While the thickness of the bilayer is fluctuating on the ns timescale, integration over time revealed that the WT sensor peptide induces a local membrane compression, which was more pronounced in the thicker bilayer with respect to both area and height (Figures 6E and 6G). In other words, the overall extent of membrane compression induced by the sensor peptide is higher in a thicker membrane. Moreover, the sensor peptide induced a substantial disordering of the lipid acyl chains, which was more pronounced in the more ordered membrane environment (Figures 6F and 6H). The membrane thickness and acyl chain order are inherently connected and any bilayer compression comes with an energetic cost (Mouritsen and Bloom, 1984; Nezil and Bloom, 1992). We speculate that minimizing these energetic costs would create a driving force for Ire1 oligomerization. When two Ire1 monomers approach one another, the compressed and disordered lipid nanodomains surrounding them coalesce (Figure 7). As a consequence, the total

region of membrane compression and acyl chain disordering diminishes, rendering a dimeric or oligomeric configuration more stable. Conversely, breaking up these oligomeric configurations of Ire1 is energetically unfavorable, with a cost that increases in thicker and more ordered bilayers. In this way, bulk physical properties of the membrane environment can determine the typical lifetime of these transient dimeric and oligomeric configurations. Prolonged physical proximity of the TMH regions of two Ire1 proteins increases the likelihood for them to establish a stable dimerization interface via the known IF1 in the lumen of the ER (Aragón et al., 2009; Credle et al., 2005). Importantly, this model is consistent with the strong negative epistasis between mutations of the IF1 or IF2 with mutations in the AH of Ire1 (Figure 3). It also explains how lipid bilayer stress can activate the UPR via the ΔIII mutant of Ire1 that cannot bind unfolded proteins (Kimata et al., 2007) (Figure 4). Our findings suggest that unfolded proteins and lipid bilayer stress jointly contribute to the activation of Ire1. The identified juxta-membrane AH represents a crucial structural element allowing Ire1 to sense adverse membrane environments and to mount the UPR. Any failure to insert the AH region into the lipid bilayer lowers the probability of Ire1 to form signaling-active oligomers, which is consistent with the array of functional defects observed for the V535R and the F531R mutant (Figures 1, 2, 3, and 4). Thus, we provide compelling evidence that bulk membrane properties contribute to the oligomerization of Ire1 and identify a juxta-membrane AH as a key structural element for Ire1's response to lipid bilayer stress.

DISCUSSION

Combining cell biology, in vitro reconstitution, and MD simulations, we establish the molecular mechanism of UPR activation by lipid bilayer stress. Ire1, the most conserved transducer of ER stress, controls UPR activity in response to various aberrant lipid compositions by sensing ER physicochemical membrane properties, rather than stably binding or recognizing individual lipid molecules. The sensing mechanism relies on a juxta-membrane AH that causes local membrane compression and acyl chain disordering. The unusual architecture of the TMH region might render Ire1 particularly sensitive to the thickness and lipid packing density of the membrane. A membrane-based modulation of the oligomeric state, conformation, and activity of membrane proteins is not unprecedented and has been reported for

CellPress

mechano-sensitive channels (Lundbaek et al., 2010), SNARE proteins (Milovanovic et al., 2015), and G protein-coupled receptors (Botelho et al., 2006; Periole et al., 2007). However, the biological and physiological context remained largely unexplored in these examples.

Here, we identify the structural element underlying the membrane responsiveness of Ire1 and show that physiologically relevant changes of the lipid packing density can significantly contribute to the oligomerization of Ire1 in vitro (Figure 5). Mutations that disrupt the AH in vitro impair the response to unfolded proteins and lipid bilayer stress in vivo (Figure 2). Numerous perturbations of lipid metabolism result in a robust activation of the UPR (Jonikas et al., 2009) and all known conditions of lipid bilayer stress exhibit a striking commonality: they are predicted to increase the membrane thickness and the molecular lipid packing density (Han et al., 2010; Lajoie et al., 2012; Pineau et al., 2009; Promlek et al., 2011; Surma et al., 2013; Thibault et al., 2012). Our MD simulations suggest that the unusual architecture of Ire1 with a juxta-membrane AH induces a substantial compression of the lipid bilayer, which is more pronounced in thicker membranes (Figures 6E and 6G). Hence, the energetic cost for membrane compression by each Ire1 molecule increases during lipid bilayer stress with the membrane thickness and the lipid packing density. However, it can be minimized by the formation of transient, dimeric configurations. These short-lived, dimeric configurations do not seem to rely on specific protein-protein interactions inside the membrane but are stabilized by the interplay of the locally compressed membrane around Ire1 with the membrane environment. The bigger the difference of membrane thickness between the compressed area and the membrane environment, the more stable these transient, dimeric configurations would be. Two Ire1 molecules that encounter each other in an unstressed membrane would have relatively little time to explore each other's surfaces and to establish a stable interaction via the large ER-lumenal and cytosolic domains before dissociation. During lipid bilayer stress, however, the two copies would remain in a dimeric configuration for increased periods of time stabilized by this membrane-based mechanism. This way, lipid bilayer stress would increase the probability of forming more stable oligomers, for example via the ER-lumenal interfaces IF1 and IF2 (van Anken et al., 2014; Aragón et al., 2009). In this sense, the membrane environment sets a timer for Ire1 to establish a stable dimerization interface. Lipid bilayer stress would provide extra stability to transient, dimeric configurations and favor Ire1 oligomerization and UPR activation. Intriguingly, the sensory mechanism of Ire1 differs fundamentally from the rotation-based mechanism of Mga2, a sensor of the lipid packing density within the hydrophobic core of the ER membrane that controls the production of unsaturated fatty acids via the essential fatty acid desaturase Ole1 (Covino et al., 2016; Ernst et al., 2016).

Our findings put Ire1 at a center stage of membrane homeostasis and reveal a molecular link between lipid metabolism and protein quality control (Puth et al., 2015; Stordeur et al., 2014). Lipid bilayer stress and unfolded proteins jointly contribute to the oligomerization of Ire1 and seem to activate the UPR in an interdependent and additive fashion. By integrating two fundamentally distinct signals, Ire1 orchestrates ER expansion with membrane

homeostasis that relies on a carefully balanced production and turnover of lipids and proteins. Our observations bear important clinical implications, as UPR activation plays an important role during viral infections and in certain types of cancer (Walter and Ron, 2011), while chronic ER stress, as seen in obesity, has been implicated in the development of insulin resistance and type 2 diabetes (Fu et al., 2011; Özcan et al., 2004). By establishing the molecular basis of UPR activation by lipid bilayer stress, we provide a new, membrane-based perspective to the role of lipids in neurodegenerative diseases and for the integrity of professional secretory cells during chronic ER stress.

Importantly, the unusual architecture in the TMH region exhibiting an AH on the ER-lumenal side of the TMH is conserved from yeast to human and also found in PERK (Figure S1). Because MD simulations provide access to short-lived processes on the ns timescale while allowing for a direct structural interpretation, we are convinced that a molecular understanding of membrane-sensitive signaling processes can be achieved best by an integrative approach of experiments and simulations. Our findings suggest that the fundamental mechanism of lipid bilayer stress sensing is conserved throughout the eukaryotic domain.

STAR★METHODS

Detailed methods are provided in the online version of this paper and include the following:

- KEY RESOURCES TABLE
- CONTACT FOR REAGENT AND RESOURCE SHARING
- EXPERIMENTAL MODEL AND SUBJECT DETAILS
  - *S. cerevisiae*
- METHOD DETAILS
  - Reagents and Peptides
  - Plasmids
  - Genetic manipulation of *S. cerevisiae*
  - Preparation of cell lysates and immunoblot analysis
  - Yeast growth assay
  - RNA preparation, cDNA synthesis, and qRT-PCR analysis
  - Subcellular fractionation and test of membrane association
  - Live cell confocal microscopy
  - Immunoprecipitation
  - CD spectroscopic measurements
  - Purification and spin labeling of the minimal sensor
  - Size-Exclusion Chromatography (SEC)
  - Liposome preparation
  - Reconstitution of the minimal sensor into liposomes
  - Carbonate extraction with proteoliposomes
  - Sucrose density gradient centrifugation
  - Hoechst33342 measurements
  - C-Laurdan spectroscopy
  - Continuous wave (cw) EPR measurements
  - Analysis of cwEPR spectra
  - MD simulations
  - Thickness and acyl chain order parameter calculation
  - MD and analysis software
- QUANTIFICATION AND STATISTICAL ANALYSIS

CellPress

SUPPLEMENTAL INFORMATION

Supplemental Information includes six figures, three tables, and two movies and can be found with this article online at http://dx.doi.org/10.1016/j.molcel.2017.06.012.

AUTHOR CONTRIBUTIONS

Conceptualization: R.E., R.C., K.H., and G.H.; Experimental Design: K.H., K.P., R.C., H.F.H., D.W., I.H., G.H., and R.E.; Performed experiments: K.H., K.P., R.C., H.F.H.; Writing – original draft: K.H., R.C., G.H., and R.E.; Writing – revised draft: K.H., K.P., R.C., D.W., I.H., G.H., and R.E.; Funding Acquisition: I.H., G.H., and R.E.; Supervision: I.H., G.H., and R.E.

ACKNOWLEDGMENTS

REFERENCES

Abraham, M.J., Murtola, T., Schulz, R., Páll, S., Smith, J.C., Hess, B., and Lindahl, E. (2015). Gromacs: High performance molecular simulations through multi-level parallelism from laptops to supercomputers. SoftwareX 1–2, 19–25.

Aragón, T., van Anken, E., Pincus, D., Serafimova, I.M., Korennykh, A.V., Rubio, C.A., and Walter, P. (2009). Messenger RNA targeting to endoplasmic reticulum stress signalling sites. Nature 457, 736–740.

Berendsen, H.J.C., Postma, J.P.M., van Gunsteren, W.F., DiNola, A., and Haak, J.R. (1984). Molecular dynamics with coupling to an external bath. J. Chem. Phys. 81, 3684–3690.

Best, R.B., Zhu, X., Shim, J., Lopes, P.E.M., Mittal, J., Feig, M., and Mackerell, A.D., Jr. (2012). Optimization of the additive CHARMM all-atom protein force field targeting improved sampling of the backbone φ, ψ and side-chain χ(1) and χ(2) dihedral angles. J. Chem. Theory Comput. 8, 3257–3273.

Bordignon, E., and Steinhoff, H.-J. (2007). Membrane protein structure and dynamics studied by site-directed spin labeling ESR. In ESR Spectroscopy in Membrane Biophysics, L.J. Hemminga and M.A. Berliner, eds. (New York: Springer Science and Business Media), pp. 129–164.

Botelho, A.V., Huber, T., Sakmar, T.P., and Brown, M.F. (2006). Curvature and hydrophobic forces drive oligomerization and modulate activity of rhodopsin in membranes. Biophys. J. 91, 4464–4477.

Bussi, G., Donadio, D., and Parrinello, M. (2007). Canonical sampling through velocity rescaling. J. Chem. Phys. 126, 014101.

Covino, R., Ballweg, S., Stordeur, C., Michaelis, J.B., Puth, K., Wernig, F., Bahrami, A., Ernst, A.M., Hummer, G., and Ernst, R. (2016). A Eukaryotic Sensor for Membrane Lipid Saturation. Mol. Cell 63, 49–59.

Cox, J.S., Shamu, C.E., and Walter, P. (1993). Transcriptional induction of genes encoding endoplasmic reticulum resident proteins requires a transmembrane protein kinase. Cell 73, 1197–1206.

Credle, J.J., Finer-Moore, J.S., Papa, F.R., Stroud, R.M., and Walter, P. (2005). On the mechanism of sensing unfolded protein in the endoplasmic reticulum. Proc. Natl. Acad. Sci. USA 102, 18773–18784.

Ernst, R., Ejsing, C.S., and Antonny, B. (2016). Homeoviscous Adaptation and the Regulation of Membrane Lipids. J. Mol. Biol. 428 (24 Pt A), 4776–4791.

Essmann, U., Perera, L., Berkowitz, M.L., Darden, T., Lee, H., and Pedersen, L.G. (1995). A smooth particle mesh Ewald method. J. Chem. Phys. 103, 8577–8593.

Fu, S., Yang, L., Li, P., Hofmann, O., Dicker, L., Hide, W., Lin, X., Watkins, S.M., Ivanov, A.R., and Hotamisligil, G.S. (2011). Aberrant lipid metabolism disrupts calcium homeostasis causing liver endoplasmic reticulum stress in obesity. Nature 473, 528–531.

Funakoshi, M., and Hochstrasser, M. (2009). Small epitope-linker modules for PCR-based C-terminal tagging in Saccharomyces cerevisiae. Yeast 26, 185–192.

Gapsys, V., de Groot, B.L., and Briones, R. (2013). Computational analysis of local membrane properties. J. Comput. Aided Mol. Des. 27, 845–858.

Gardner, B.M., and Walter, P. (2011). Unfolded proteins are Ire1-activating ligands that directly induce the unfolded protein response. Science 333, 1891–1894.

Gautier, R., Douguet, D., Antonny, B., and Drin, G. (2008). HELIQUEST: a web server to screen sequences with specific α-helical properties. Bioinformatics 24, 2101–2102.

Gueldener, U., Heinisch, J., Koehler, G.J., Voss, D., and Hegemann, J.H. (2002). A second set of loxP marker cassettes for Cre-mediated multiple gene knockouts in budding yeast. Nucleic Acids Res. 30, e23.

Han, S., Lone, M.A., Schneiter, R., and Chang, A. (2010). Orm1 and Orm2 are conserved endoplasmic reticulum membrane proteins regulating lipid homeostasis and protein quality control. Proc. Natl. Acad. Sci. USA 107, 5851–5856.

Hess, B., Kutzner, C., van der Spoel, D., and Lindahl, E. (2008). GROMACS 4:Algorithms for Highly Efficient, Load-Balanced, and Scalable Molecular Simulation. J. Chem. Theory Comput. 4, 435–447.

Humphrey, W., Dalke, A., and Schulten, K. (1996). VMD: visual molecular dynamics. J. Mol. Graph. 14, 33–38, 27–28.

Hunter, J.D. (2007). Matplotlib: A 2D graphics environment. Comput. Sci. Eng. 9, 99–104.

Jo, S., Kim, T., and Im, W. (2007). Automated builder and database of protein/membrane complexes for molecular dynamics simulations. PLoS ONE 2, e880.

Jo, S., Kim, T., Iyer, V.G., and Im, W. (2008). CHARMM-GUI: a web-based graphical user interface for CHARMM. J. Comput. Chem. 29, 1859–1865.

Jo, S., Lim, J.B., Klauda, J.B., and Im, W. (2009). CHARMM-GUI Membrane Builder for mixed bilayers and its application to yeast membranes. Biophys. J. 97, 50–58.

Jo, S., Cheng, X., Islam, S.M., Huang, L., Rui, H., Zhu, A., Lee, H.S., Qi, Y., Han, W., Vanommeslaeghe, K., et al. (2014). CHARMM-GUI PDB manipulator for advanced modeling and simulations of proteins containing nonstandard residues. Adv. Protein Chem. Struct. Biol. 96, 235–265.

Jonikas, M.C., Collins, S.R., Denic, V., Oh, E., Quan, E.M., Schmid, V., Weibezahn, J., Schwappach, B., Walter, P., Weissman, J.S., and Schuldiner, M. (2009). Comprehensive characterization of genes required for protein folding in the endoplasmic reticulum. Science 323, 1693–1697.

Kaiser, H.J., Surma, M.A., Mayer, F., Levental, I., Grzybek, M., Klemm, R.W., Da Cruz, S., Meisinger, C., Müller, V., Simons, K., and Lingwood, D. (2011). Molecular convergence of bacterial and eukaryotic surface order. J. Biol. Chem. 286, 40631–40637.

Kimata, Y., and Kohno, K. (2011). Endoplasmic reticulum stress-sensing mechanisms in yeast and mammalian cells. Curr. Opin. Cell Biol. 23, 135–142.

Kimata, Y., Oikawa, D., Shimizu, Y., Ishiwata-Kimata, Y., and Kohno, K. (2004). A role for BiP as an adjustor for the endoplasmic reticulum stress-sensing protein Ire1. J. Cell Biol. 167, 445–456.

Kimata, Y., Ishiwata-Kimata, Y., Ito, T., Hirata, A., Suzuki, T., Oikawa, D., Takeuchi, M., and Kohno, K. (2007). Two regulatory steps of ER-stress sensor Ire1 involving its cluster formation and interaction with unfolded proteins. J. Cell Biol. 179, 75–86.

Klauda, J.B., Venable, R.M., Freites, J.A., O'Connor, J.W., Tobias, D.J., Mondragon-Ramirez, C., Vorobyov, I., MacKerell, A.D., Jr., and Pastor, R.W.

(2010). Update of the CHARMM all-atom additive force field for lipids: validation on six lipid types. J. Phys. Chem. B *114*, 7830–7843.

Klemm, R.W., Ejsing, C.S., Surma, M.A., Kaiser, H.J., Gerl, M.J., Sampaio, J.L., de Robillard, Q., Ferguson, C., Proszynski, T.J., Shevchenko, A., and Simons, K. (2009). Segregation of sphingolipids and sterols during formation of secretory vesicles at the trans-Golgi network. J. Cell Biol. *185*, 601–612.

Klose, C., Ejsing, C.S., García-Sáez, A.J., Kaiser, H.J., Sampaio, J.L., Surma, M.A., Shevchenko, A., Schwille, P., and Simons, K. (2010). Yeast lipids can phase-separate into micrometer-scale membrane domains. J. Biol. Chem. *285*, 30224–30232.

Lajoie, P., Moir, R.D., Willis, I.M., and Snapp, E.L. (2012). Kar2p availability defines distinct forms of endoplasmic reticulum stress in living cells. Mol. Biol. Cell *23*, 955–964.

Lee, J., Cheng, X., Swails, J.M., Yeom, M.S., Eastman, P.K., Lemkul, J.A., Wei, S., Buckner, J., Jeong, J.C., Qi, Y., et al. (2016). CHARMM-GUI Input Generator for NAMD, GROMACS, AMBER, OpenMM, and CHARMM/OpenMM Simulations Using the CHARMM36 Additive Force Field. J. Chem. Theory Comput. *12*, 405–413.

Lundbaek, J.A., Collingwood, S.A., Ingólfsson, H.I., Kapoor, R., and Andersen, O.S. (2010). Lipid bilayer regulation of membrane protein function: gramicidin channels as molecular force probes. J. R. Soc. Interface *7*, 373–395.

Merksamer, P.I., Trusina, A., and Papa, F.R. (2008). Real-time redox measurements during endoplasmic reticulum stress reveal interlinked protein folding functions. Cell *135*, 933–947.

Michaud-Agrawal, N., Denning, E.J., Woolf, T.B., and Beckstein, O. (2011). MDAnalysis: a toolkit for the analysis of molecular dynamics simulations. J. Comput. Chem. *32*, 2319–2327.

Milovanovic, D., Honigmann, A., Koike, S., Göttfert, F., Pähler, G., Junius, M., Müllar, S., Diederichsen, U., Janshoff, A., Grubmüller, H., et al. (2015). Hydrophobic mismatch sorts SNARE proteins into distinct membrane domains. Nat. Commun. *6*, 5984.

Mori, K. (2009). Signalling pathways in the unfolded protein response: development from yeast to mammals. J. Biochem. *146*, 743–750.

Mori, K., Ma, W., Gething, M.J., and Sambrook, J. (1993). A transmembrane protein with a cdc2+/CDC28-related kinase activity is required for signaling from the ER to the nucleus. Cell *74*, 743–756.

Mori, K., Kawahara, T., Yoshida, H., Yanagi, H., and Yura, T. (1996). Signalling from endoplasmic reticulum to nucleus: transcription factor with a basic-leucine zipper motif is required for the unfolded protein-response pathway. Genes Cells *1*, 803–817.

Mouritsen, O.G., and Bloom, M. (1984). Mattress model of lipid-protein interactions in membranes. Biophys. J. *46*, 141–153.

Nezil, F.A., and Bloom, M. (1992). Combined influence of cholesterol and synthetic amphiphillic peptides upon bilayer thickness in model membranes. Biophys. J. *61*, 1176–1183.

Özcan, U., Cao, Q., Yilmaz, E., Lee, A.-H., Iwakoshi, N.N., Ozdelen, E., Tuncman, G., Görgün, C., Glimcher, L.H., and Hotamisligil, G.S. (2004). Endoplasmic reticulum stress links obesity, insulin action, and type 2 diabetes. Science *306*, 457–461.

Parrinello, M., and Rahman, A. (1980). Crystal structure and pair potentials: A molecular-dynamics study. Phys. Rev. Lett. *45*, 1196–1199.

Pérez, F., and Granger, B.E. (2007). IPython: A system for interactive scientific computing. Comput. Sci. Eng. *9*, 21–29.

Periole, X., Huber, T., Marrink, S.J., and Sakmar, T.P. (2007). G protein-coupled receptors self-assemble in dynamics simulations of model bilayers. J. Am. Chem. Soc. *129*, 10126–10132.

Pettersen, E.F., Goddard, T.D., Huang, C.C., Couch, G.S., Greenblatt, D.M., Meng, E.C., and Ferrin, T.E. (2004). UCSF Chimera–a visualization system for exploratory research and analysis. J. Comput. Chem. *25*, 1605–1612.

Pincus, D., Chevalier, M.W., Aragón, T., van Anken, E., Vidal, S.E., El-Samad, H., and Walter, P. (2010). BiP binding to the ER-stress sensor Ire1 tunes the homeostatic behavior of the unfolded protein response. PLoS Biol. *8*, e1000415.

Pineau, L., Colas, J., Dupont, S., Beney, L., Fleurat-Lessard, P., Berjeaud, J.M., Bergès, T., and Ferreira, T. (2009). Lipid-induced ER stress: synergistic effects of sterols and saturated fatty acids. Traffic *10*, 673–690.

Plumb, R., Zhang, Z.-R., Appathurai, S., and Mariappan, M. (2015). A functional link between the co-translational protein translocation pathway and the UPR. eLife *4*, e07426.

Promlek, T., Ishiwata-Kimata, Y., Shido, M., Sakuramoto, M., Kohno, K., and Kimata, Y. (2011). Membrane aberrancy and unfolded proteins activate the endoplasmic reticulum stress sensor Ire1 in different ways. Mol. Biol. Cell *22*, 3520–3532.

Pronk, S., Páll, S., Schulz, R., Larsson, P., Bjelkmar, P., Apostolov, R., Shirts, M.R., Smith, J.C., Kasson, P.M., van der Spoel, D., et al. (2013). GROMACS 4.5: a high-throughput and highly parallel open source molecular simulation toolkit. Bioinformatics *29*, 845–854.

Puth, K., Hofbauer, H.F., Sáenz, J.P., and Ernst, R. (2015). Homeostatic control of biological membranes by dedicated lipid and membrane packing sensors. Biol. Chem. *396*, 1043–1058.

Sidrauski, C., and Walter, P. (1997). The transmembrane kinase Ire1p is a site-specific endonuclease that initiates mRNA splicing in the unfolded protein response. Cell *90*, 1031–1039.

Stordeur, C., Puth, K., Sáenz, J.P., and Ernst, R. (2014). Crosstalk of lipid and protein homeostasis to maintain membrane function. Biol. Chem. *395*, 313–326.

Surma, M.A., Klose, C., Peng, D., Shales, M., Mrejen, C., Stefanko, A., Braberg, H., Gordon, D.E., Vorkel, D., Ejsing, C.S., et al. (2013). A lipid E-MAP identifies Ubx2 as a critical regulator of lipid saturation and lipid bilayer stress. Mol. Cell *51*, 519–530.

Thibault, G., Shui, G., Kim, W., McAlister, G.C., Ismail, N., Gygi, S.P., Wenk, M.R., and Ng, D.T. (2012). The membrane stress response buffers lethal effects of lipid disequilibrium by reprogramming the protein homeostasis network. Mol. Cell *48*, 16–27.

Tirasophon, W., Welihinda, A.A., and Kaufman, R.J. (1998). A stress response pathway from the endoplasmic reticulum to the nucleus requires a novel bifunctional protein kinase/endoribonuclease (Ire1p) in mammalian cells. Genes Dev. *12*, 1812–1824.

Travers, K.J., Patil, C.K., Wodicka, L., Lockhart, D.J., Weissman, J.S., and Walter, P. (2000). Functional and genomic analyses reveal an essential coordination between the unfolded protein response and ER-associated degradation. Cell *101*, 249–258.

van Anken, E., Pincus, D., Coyle, S., Aragón, T., Osman, C., Lari, F., Gómez Puerta, S., Korennykh, A.V., and Walter, P. (2014). Specificity in endoplasmic reticulum-stress signaling in yeast entails a step-wise engagement of HAC1 mRNA to clusters of the stress sensor Ire1. eLife *3*, e05031.

Van Der Spoel, D., Lindahl, E., Hess, B., Groenhof, G., Mark, A.E., and Berendsen, H.J. (2005). GROMACS: fast, flexible, and free. J. Comput. Chem. *26*, 1701–1718.

Van Der Walt, S., Colbert, S.C., and Varoquaux, G. (2011). The NumPy array: a structure for efficient numerical computation. Comput. Sci. Eng. *13*, 22–30.

Vanommeslaeghe, K., Hatcher, E., Acharya, C., Kundu, S., Zhong, S., Shim, J., Darian, E., Guvench, O., Lopes, P., Vorobyov, I., and Mackerell, A.D., Jr. (2010). CHARMM general force field: A force field for drug-like molecules compatible with the CHARMM all-atom additive biological force fields. J. Comput. Chem. *31*, 671–690.

Volmer, R., van der Ploeg, K., and Ron, D. (2013). Membrane lipid saturation activates endoplasmic reticulum unfolded protein response transducers through their transmembrane domains. Proc. Natl. Acad. Sci. USA *110*, 4628–4633.

Walter, P., and Ron, D. (2011). The unfolded protein response: from stress pathway to homeostatic regulation. Science *334*, 1081–1086.

Wu, E.L., Cheng, X., Jo, S., Rui, H., Song, K.C., Dávila-Contreras, E.M., Qi, Y., Lee, J., Monje-Galvan, V., Venable, R.M., et al. (2014). CHARMM-GUI Membrane Builder toward realistic biological membrane simulations. J. Comput. Chem. *35*, 1997–2004.

CellPress

STAR★METHODS

KEY RESOURCES TABLE

REAGENT or RESOURCE	SOURCE	IDENTIFIER
Antibodies		
anti-FLAG monoclonal (M2)	Sigma Aldrich	F3165; RRID: AB_259529
anti-HA monoclonal (3F10)	Sigma Aldrich	ROAHAHA ROCHE
anti-Dpm1 monoclonal (5C5A7)	VWR	ABNOMAB14032
anti-Pgk1 (22C5D8)	VWR	ABCAAB113687-250
anti-MBP monoclonal	NEB	E8032L; RRID: AB_1559730
anti-Kar2 polyclonal (y-115)	Santa Cruz	sc-33630; RRID: AB_672118
anti-mouse-HRP	Dianova	115-035-003
anti-rat-HRP	Dianova	112-035-003
Chemicals, Peptides, and Recombinant Proteins		
Biotin-KNQNSLLLKFGSLVYRIIETGV-CONH$_2$	ZIK B CUBE TU Dresden	Ire1$^{522-543}$ WT
Biotin-KNQNSLLLKRGSLVYRIIETGV-CONH$_2$	ZIK B CUBE TU Dresden	Ire1$^{522-543}$ F531R
Biotin-KNQNSLLLKFGSLRYRIIETGV-CONH$_2$	ZIK B CUBE TU Dresden	Ire1$^{522-543}$ V535R
Critical Commercial Assays		
Q5 Site-Directed Mutagenesis Kit	NEB	E0554S
QuikChange Site-Directed Mutagenesis Kit	Agilent Technologies	#200524
PHUSION High-Fidelity DNA Polymerase	NEB	M0530L
RNeasy Plus RNA Isolation Kit	QIAGEN	74106
Superscript II RT	ThermoFisher	18064014
Experimental Models: Organisms/Strains		
BY4741 MATa; his3Δ1; leu2Δ0; met15Δ0; ura3Δ0	Euroscarf	N/A
BY4741 MATa; his3Δ1; leu2Δ0; met15Δ0; ura3Δ0; ire1Δ::kanMX4	Euroscarf	N/A
BY4741 MATa; his3Δ1; leu2Δ0; met15Δ0; ura3Δ0; ire1Δ::URA pUG72	This paper	pUG72
BY4741 MATa; his3Δ1; leu2Δ0; met15Δ0; ura3Δ0; ire1Δ::URA IRE1-3xHA-GFP::HIS pRE451	This paper	pRE451
BY4741 MATa; his3Δ1; leu2Δ0; met15Δ0; ura3Δ0; ire1Δ::URA IRE1-3xHA-GFP::HIS pRE455	This paper	pRE455
BY4741 MATa; his3Δ1; leu2Δ0; met15Δ0; ura3Δ0; ire1Δ::URA IRE1-3xHA-GFP::HIS pRE458	This paper	pRE458
BY4741 MATa; his3Δ1; leu2Δ0; met15Δ0; ura3Δ0; ire1Δ::URA IRE1-3xHA-GFP::HIS pRE465	This paper	pRE465
BY4741 MATa; his3Δ1; leu2Δ0; met15Δ0; ura3Δ0; ire1Δ::URA IRE1-3xHA-GFP::HIS pRE551	This paper	pRE551
BY4741 MATa; his3Δ1; leu2Δ0; met15Δ0; ura3Δ0; ire1Δ::URA IRE1-3xHA-GFP::HIS pRE553	This paper	pRE553
BY4741 MATa; his3Δ1; leu2Δ0; met15Δ0; ura3Δ0; ire1Δ::URA IRE1-3xHA-GFP::HIS pRE555	This paper	pRE555
BY4741 MATa; his3Δ1; leu2Δ0; met15Δ0; ura3Δ0; ire1Δ::URA IRE1-3xHA-GFP::HIS pRE556	This paper	pRE556
BY4741 MATa; his3Δ1; leu2Δ0; met15Δ0; ura3Δ0; ire1Δ::URA SEC63-FLAG::kanMX4 pRE451	This paper	pRE451
BY4741 MATa; his3Δ1; leu2Δ0; met15Δ0; ura3Δ0; ire1Δ::URA SEC63-FLAG::kanMX4 pRE551	This paper	pRE551
BY4741 MATa; his3Δ1; leu2Δ0; met15Δ0; ura3Δ0; ire1Δ::URA SEC63-FLAG::kanMX4 pRE556	This paper	pRE556

(Continued on next page)

Continued

REAGENT or RESOURCE	SOURCE	IDENTIFIER
BY4741 MATa; his3Δ1; leu2Δ0; met15Δ0; ura3Δ0; ire1Δ::URA IRE1-3xHA-GFP::HIS pRE655	This paper	pRE655
BY4741 MATa; his3Δ1; leu2Δ0; met15Δ0; ura3Δ0; ire1Δ::kanMX4 IRE1-3xHA-GFP::LEU pRE488	This paper	pRE488
Oligonucleotides		
Oligo(dt) Primer	ThermoFisher	18418012
*HAC1*spliced forward primer: 5′-GCGTAATCCAGAAGCGCAGT-3′	Sigma-Aldrich	N/A
*HAC1*spliced reverse primer: 5′-GTGATGAAGAAATCATTCAATTCAAATG-3′	Sigma-Aldrich	N/A
PDI1 forward primer: 5′-GATCGATTACGAGGGACCTAGA-3′	Sigma-Aldrich	N/A
PDI1 reverse primer: 5′-GCGGAGGGCAAGTAAATAGAA-3′	Sigma-Aldrich	N/A
ACT1 forward primer: 5′-TGTCACCAACTGGGACGATA-3′	Sigma-Aldrich	N/A
ACT1 reverse primer: 5′-AACCAGCGTAAATTGGAACG-3′	Sigma-Aldrich	N/A
*IRE1*prom*IRE1* knockout forward primer: 5′-GCTTTTAGGGACAGTTCTATTCTTCCAACGTGCGAAGCGTTCCAACAGCTGAAGCTTCGTACGC-3′	Sigma-Aldrich	N/A
*IRE1*prom*IRE1* knockout reverse primer: 5′-TTAATGCAATAATCAACCAAGAAGAAGCAGAGGGGCATGAACATGGCATAGGCCACTAGTGGATCTG-3′	Sigma-Aldrich	N/A
Recombinant DNA		
pRS315-IRE1-GFP WT	van Anken et al., 2014	pEvA200
pUG72	Gueldener et al., 2002	pRE211
pcDNA3.1-IRE1-3xHA-GFP WT	This paper	pRE451
pcDNA3.1-IRE1-3xHA-GFP IF2 (W426A)	This paper	pRE455
pcDNA3.1-IRE1-3xHA-GFP IF1 (T226A F247A)	This paper	pRE465
pcDNA3.1-IRE1-3xHA-GFP V535R	This paper	pRE551
pcDNA3.1-IRE1-3xHA-GFP V535R, IF1	This paper	pRE553
pcDNA3.1-IRE1-3xHA-GFP V535R, IF2	This paper	pRE555
pcDNA3.1-IRE1-3xHA-GFP F531R	This paper	pRE556
pcDNA3.1-IRE1-3xHA-GFP ΔIII	This paper	pRE458
pcDNA3.1-IRE1-3xHA-GFP ΔIII V535R	This paper	pRE655
pFA6a-6xGLY-3xFLAG-kanMX6	Funakoshi and Hochstrasser, 2009	pRE170
pMAL-C2x	NEB	N/A
MBP-IRE1-TMH WT	This paper	pRE424
MBP-IRE1-TMH C552S	This paper	pRE431
MBP-IRE1-TMH F531R	This paper	pRE629
MBP-IRE1-TMH C552S L534C	This paper	pRE566
MBP-IRE1-TMH C552S V535C	This paper	pRE567
MBP-IRE1-TMH C552S Y536C	This paper	pRE568
MBP-IRE1-TMH C552S R537C	This paper	pRE432
MBP-IRE1-TMH C552S I538C	This paper	pRE433
MBP-IRE1-TMH C552S I539C	This paper	pRE434
Software and Algorithms		
GROMACS 5	Abraham et al., 2015; Hess et al., 2008; Pronk et al., 2013; Van Der Spoel et al., 2005	N/A
IPython	Pérez and Granger, 2007	N/A
Matplotlib	Hunter, 2007	N/A
NumPy	Van Der Walt et al., 2011	N/A

CellPress

Continued

REAGENT or RESOURCE	SOURCE	IDENTIFIER
MDAnalysis	Michaud-Agrawal et al., 2011	N/A
VMD	Humphrey et al., 1996	N/A
g_lomepro v1.0.2 tool	Gapsys et al., 2013	N/A
Other		
PCR grade dNTP mix	ThermoFisher	18427013
Absolute QPCR Mix, SYBR green	ThermoFisher	AB1159A

CONTACT FOR REAGENT AND RESOURCE SHARING

Further information and requests for resources and reagents should be directed to and will be fulfilled by the Lead Contact, Robert Ernst (robert.ernst@uks.eu).

EXPERIMENTAL MODEL AND SUBJECT DETAILS

S. cerevisiae

Strains used in this study and information regarding their genotype can be found in the Key Resources Table and in Table S1. Strains were cultivated on SCD complete or selection plates at 30°C. If not stated otherwise, a liquid culture was inoculated with a single colony and cultured in YPD, SCD complete or SCD selection media overnight, until the cells reached the stationary phase. The overnight culture was used to inoculate a fresh culture to an $OD_{600} = 0.2$ in the required medium and cultivated to the mid-exponential phase ($OD_{600} = 1.0$). If indicated, the medium was supplemented with DTT from a 1M stock. For inositol depletion, cells from an overnight culture in SCD and in mid-exponential phase were washed with SCD media lacking inositol and used to inoculate a fresh culture in SCD lacking inositol. Additional adaptations to this general procedure are provided in the METHOD DETAILS section.

METHOD DETAILS

Reagents and Peptides

All chemicals and reagents used in this study were purchased from Sigma Aldrich and of analytical or higher grade. Synthetic biotinylated peptides were purchased from ZIK B CUBE (TU Dresden) and purified to > 90% purity. The supplier verified peptide quality utilizing mass spectrometry. The following peptides were used:

$Ire1^{522-543}$ WT (Biotin-KNQNSLLLKFGSLVYRIIETGV-CONH$_2$)
$Ire1^{522-543}$ F531R (Biotin-KNQNSLLLK**R**GSLVYRIIETGV-CONH$_2$)
$Ire1^{522-543}$ V535R (Biotin-KNQNSLLLKFGSL**R**YRIIETGV-CONH$_2$)

Plasmids

All plasmids used in this study can be found in the Key Resources Table and are listed in Table S2.

Genetic manipulation of *S. cerevisiae*

Construction of a *ΔIRE1* strain: Based on a previously established strategy the pUG72-URA deletion cassette was amplified using the *IRE1*prom*IRE1* knockout forward and reverse primer in order to remove both the *IRE1* promotor (−1 to −551 bp) and the *IRE1* gene from the genome (Gueldener et al., 2002).

Construction of an *IRE1* knock-in construct: A His3MX6 marker cassette flanked at the 3′ end by a sequence from the endogenous *IRE1* locus (for genomic insertion of the knock-in construct) was synthesized and amplified by PCR including *Hind*III/*BamH*I restriction sites and cloned into the pcDNA3.1 (+) vector. Subsequently, the sequence of *IRE1-GFP* including the endogenous promoter of *IRE1* (−1 to −551 bp) and the endogenous 5′ terminator sequence were amplified from pEvA200 (van Anken et al., 2014) by PCR and equipped with *BamH*I/*Xho*I restriction sites for cloning into pcDNA3.1 (+). A preexisting C-terminal 1xHA-tag-encoding sequence was removed from the resulting plasmid, and a 3xHA-tag-encoding sequence was introduced using the Q5 site-directed mutagenesis kit (NEB) at the position H875 to yield pcDNA3.1-*IRE1*$_{3xHA-GFP}$. Site-directed mutagenesis of this plasmid was performed using a PCR-based strategy based on the QuikChange® method (Stratagene) using PHUSION polymerase (NEB). Deletion, exchange or introduction of DNA sequences > 6bp was performed using the Q5 site-directed mutagenesis kit (NEB). For subsequent transformation of *S. cerevisiae* YRE127, the knock-in plasmid was linearized using *Hind*III and *Xho*I restriction enzymes. All mutant variants are listed in the Key Resources Table.

CellPress

In analogy to the knock-in construct, a *CEN*-based construct was cloned based on the pPW1628/pEvA200 plasmid (van Anken et al., 2014) by deletion of the C-terminal 1xHA-tag-encoding sequence and subsequent introduction of a 3xHA-tag-encoding sequence utilizing the Q5 site-directed mutagenesis kit (NEB) to yield pRE488.

C-terminal tagging: *SEC63* was equipped with a 3xFLAG-tag by using the pFA6a-6xGly-3xFLAG-kanMX6 plasmid (Funakoshi and Hochstrasser, 2009).

Preparation of cell lysates and immunoblot analysis

Cells were cultivated from OD_{600} = 0.2 to the mid-exponential phase OD_{600} = 1.0 and 20 OD equivalents were harvested by centrifugation, washed with phosphate-buffered saline (PBS), and snap frozen. Cells were lysed in 1 mL lysis buffer (PBS, 10 μg/ml chymostatin, 10 μg/ml antipain, 10 μg/ml pepstatin) by bead beating with zirconia beads (Roth) for 5 min at 4°C. The cell lysate was mixed with 5x reducing sample buffer (8 M urea, 0.1 M Tris-HCl pH 6.8, 5 mM EDTA, 3.2% (w/v) SDS, 0.15% (w/v) bromphenol blue, 4% (v/v) glycerol, 4% (v/v) β-mercaptoethanol) at a ratio of 5:1 and heated at 95°C for 10 min. Proteins were subjected to 4%–15% Mini-PROTEAN-TGX gels (BioRad) and separated by SDS-PAGE. For subsequent immunoblotting, proteins were transferred to methanol-activated PVDF membranes using semi-dry Western-blotting. Specific proteins were detected using antigen-specific primary antibodies, HRP-coupled secondary antibodies, and chemiluminescence.

Yeast growth assay

Overnight pre-cultures of the desired yeast strains were used to inoculate fresh cultures in either SCD complete or YPD to an OD_{600} of 0.2. The cells were cultivated for 5-6 hr at 30°C. Then, the culture was diluted back to an OD_{600} = 0.05 using pre-warmed medium. 50 μl of these cultures were used to inoculate cultures in a 96-well plate, containing 180 μl of either SCD complete (minimal medium) or YPD (rich medium) and 20 μl of a DTT dilution row. The cells were cultivated for 18 hr at 30°C in the 96-well plate without agitation and carefully mixed only prior to the determination of the OD_{600} a 96-well plate-compatible photospectrometer.

RNA preparation, cDNA synthesis, and qRT-PCR analysis

A 30 ml-culture inoculated from a single colony of the required yeast strains was cultivated over night to the mid-exponential phase and used to inoculate a fresh culture of 30 mL to an OD_{600} = 0.2. In order to induce lipid bilayer stress by inositol depletion, the cells were thoroughly washed with inositol-depleted medium before cultivation in inositol-depleted medium for an additional 3 hr. In order to induce massive ER-stress, the cells were first cultivated in YPD for 3h and then stressed by adjusting the medium to 4 mM DTT and further cultivation for 1 hr (in the experiments for Figure 4 with the ΔIII mutant of Ire1 all analyzed strains were stressed for 30 min). After cultivation, 5 OD_{600} equivalents were harvested by centrifugation, washed with PBS and snap frozen in liquid N_2. Total RNA was extracted and treated with DNase using the RNeasy Plus RNA Isolation Kit (QIAGEN). cDNA was synthesized from 500 ng isolated total RNA using oligo(dt)12-18 primers (0.5 μg), PCR grade dNTP mix (0.5 μM) First Strand Buffer (1x), DTT (10mM) and Superscript™ II RT (Invitrogen). Quantitative real-time PCR was performed using Absolute qPCR SYBR Green Mix (Thermo Scientific) in a PikoReal Real-time PCR system (Thermo Scientific). The DNA of interest was amplified using the following primers:

> $HAC1_{spliced}$ forward primer: 5′-GCGTAATCCAGAAGCGCAGT-3′
> $HAC1_{spliced}$ reverse primer: 5′-GTGATGAAGAAATCATTCAATTCAAATG-3′
> *PDI1* forward primer: 5′-GATCGATTACGAGGGACCTAGA-3′
> *PDI1* reverse primer: 5′-GCGGAGGGCAAGTAAATAGAA-3′
> *ACT1* forward primer: 5′-TGTCACCAACTGGGACGATA-3′
> *ACT1* reverse primer: 5′-AACCAGCGTAAATTGGAACG-3′.

All reactions were performed with technical duplicates and at least biological triplicates. Non-template controls (RNA) and non-reaction controls (H_2O) were routinely performed. The qPCR program included Step 1: 95°C, 15 min; Step 2: 95°C, 20 s; Step 3: 58°C, 20 s; Step 4: 72°C, 30 s, Step 5: 72°C, 5 min; the steps 2-4 were carried out in 40 cycles. Relative quantification was performed after normalization to *ACT1* levels based on the comparative ΔΔ*CT* method (StepOnePlus™ user Manual, Applied Biosysytems).

Subcellular fractionation and test of membrane association

For membrane fractionation, 80 OD_{600} equivalents of cells grown in YPD to the mid-exponential phase (OD_{600}) were harvested by centrifugation, washed with PBS and rapidly frozen. All subsequent steps were performed at 4°C. The cell pellets were resuspended in 1 mL lysis buffer (50 mM HEPES, pH 7.4, 150 mM NaCl, 1 mM EDTA, 10 μg/ml chymostatin, 10 μg/ml antipain, 10 μg/ml pepstatin) and disrupted by bead beating with zirconia beads (Roth) for 5 × 1 min. Cell debris was removed by centrifugation (5 min, 800x g) and the cleared lysate was further centrifuged (10 min, 5,000x g). The remaining supernatant was divided into equal parts and mixed with an equal volume of lysis buffer supplemented with 0.2 M Na_2CO_3 (pH 11.0), 2% Triton X-100, 5 M urea or without further additives, and incubated for 1 hr on an overhead rotator. Subsequently, the samples were centrifuged (45 min, 100,000x g) to separate soluble proteins and membrane-associated proteins for further analysis using SDS-PAGE and immunoblotting.

Live cell confocal microscopy

If not stated otherwise, cells were grown to mid-exponential growth phase as previously described. Cells were depleted for inositol by cultivation in inositol-depleted medium for 3 hr. Massive ER-stress was induced by cultivating the cells in SCD for 1.5 hr in medium containing 10 mM DTT. Prior to live imaging, the cells were immobilized on microscopic slides coated with the respective media containing 2% agar. Microscopy was performed using a Zeiss LSM 780 and Zeiss LSM 880 confocal laser scanning microscope (Carl Zeiss AG) with spectral detection and a Plan-Apochromat 63 × 1.40 NA oil immersion objective. GFP fluorescence was excited at 488 nm and the emission was detected between 500 and 600 nm. Transmission images were simultaneously recorded using differential interference contrast (DIC) optics.

Cells expressing WT and mutant variants of Ire1$_{3xHA-GFP}$ were analyzed and Ire1-positive clusters were identified using automated scripts (as outlined below). For cells stressed with 10 mM DTT, z stacks (240 nm step-size) were recorded using 2% laser power to minimize bleaching and merged to z-projections (high intensity clusters). The image threshold was set to 160/255 to result a b/w picture identifying fluorescent clusters of Ire1$_{3xHA-GFP}$. Selected clusters were analyzed utilizing the 'analyze particles' function in Fiji counting all particles meeting set criteria (size: 4-infinity px; circularity: 0-1; including holes). For cells grown under inositol depletion conditions, microscopic images were recorded using 10% laser power and one confocal plane was monitored through the center of the cells (low intensity clusters). For Ire1 cluster analysis, the image threshold was set to 52/255. The number of cells was determined manually and dead cells were omitted from the analysis.

Immunoprecipitation

For immunoprecipitation, 50 OD$_{600}$ equivalents of cells grown in YPD to the mid-exponential phase (OD$_{600}$) were harvested by centrifugation, washed with PBS and rapidly frozen. All subsequent steps were performed at 4°C. The cells were resuspended in 1 mL lysis buffer (50 mM HEPES, pH 7.4, 150 mM NaCl, 1 mM EDTA, 10 μg/ml chymostatin, 10 μg/ml antipain, 10 μg/ml pepstatin) and disrupted by bead beating with zirconia beads (Roth) for 5 × 1 min. Cell debris was removed by centrifugation (5 min, 800x g) and the cleared lysate was adjusted to 1% digitonin (Sec63 co-IP) or 1% Triton X-100 (Kar2/BiP co-IP) for solubilization. After 1 hr incubation on an overhead rotator, the non-solubilized material was removed by centrifugation (10 min, 21,000x g). The supernatant was subjected to immunoprecipitation. HA-tagged and FLAG-tagged were retrieved using 20 μl anti-HA high affinity matrix slurry (Roche) and 20 μl EZview™ Red ANTI-FLAG® M2 affinity Gel beads, respectively. After an incubation of > 3h on an overhead rotator, the affinity matrix was thoroughly washed with IP buffer (50 mM HEPES, pH 7.4, 150 mM NaCl, 1 mM EDTA, 0.1% of respective detergent). The immunoprecipitated proteins were eluted using 5x reducing sample buffer at a ratio of 5:2 for further analysis via SDS-PAGE and immunoblotting.

CD spectroscopic measurements

CD spectroscopy was performed on a J-715 spectropolarimeter (Jasco). Peptides were measured at a concentration of 20 μM in the presence and absence of 1% DDM (w/v) in 20 mM sodium phosphate buffer, pH 7.0. Experiments were performed at room temperature in a HELLMA quartz cell with an optical path length of 0.01 cm. Each spectrum was obtained by averaging several scans recorded from 190 to 260 nm with a bandwidth of 2nm, a step of 1nm and a scan speed of 20 nm/min. All spectra were blanked to their respective buffers.

Purification and spin labeling of the minimal sensor

The minimal sensor-encoding region of *IRE1* (corresponding to the Ire1$^{F526–L561}$) was cloned into the pMAL-C2x *E. coli* expression vector (NEB) to encode for a fusion protein of the Maltose-binding protein and Ire1$^{F526–L561}$ (referred to as minimal sensor). *E. coli* BL21(DE3)pLysS served as expression host for the heterologous overproduction of the minimal sensor and its mutant variants. All mutant variants used for this study are listed in the Key Resources Table. For expression, 2 l of LB-rich medium (LB medium supplemented with 2% glucose, 100 μg/ml ampicillin and 34 μg/ml chloramphenicol) was inoculated 1:50 with an overnight culture and cultivated at 37°C under constant agitation, until an OD$_{600}$ = 0.6 was reached. Protein production was induced adjusting the medium to 0.3 mM isopropyl-β-D-thiogalactopyranoside (IPTG) and further cultivation at 37°C for 3 hr. The cells were harvested by centrifugation. Cell pellets could be stored at −20°C. All further steps were carried out at 4°C. The cells were thawed and resuspended in 10 mL lysis buffer (50 mM HEPES, pH 7.4, 150 mM NaCl, 1 mM EDTA, 10 μg/ml chymostatin, 10 μg/ml antipain, 10 μg/ml pepstatin, 2 mM DTT, 5 U/ml benzonase) per liter of expression culture and disrupted by sonication (3 × 60 s, amplitude 30%, 70% duty cycle). To increase the yield and to solubilize the MBP-Ire1^{AH+TMH} fusion protein, the lysate was adjusted to 50 mM n-octyl-β-D-glucopyranoside (β-OG) and incubated for 10 min while gently shaking. Cell debris and non-solubilized material was removed by centrifugation (30 min, 100,000x g) and the supernatant was applied to a 1.5 mL amylose resin (NEB) per liter of expression culture. The column was washed with 20 column volumes (CV) of wash buffer 1 (50 mM HEPES, pH 7.4, 150 mM NaCl, 1 mM EDTA, 50 mM β-OG, 1 mM TCEP), followed by 20 CV of wash buffer 2 (50 mM HEPES, pH 7.4, 150 mM NaCl, 1 mM EDTA, 50 mM β-OG) to remove reducing agents. Cysteine residues of the minimal sensor were labeled on the column by incubation with 1 mM (1-oxyl-2,2,5,5-tetramethyl-pyrroline-3-methyl)methanethio-sulfonate (MTS-SL; Enzo Life Sciences) spin label for 4 hr under constant agitation. Excess spin label was removed with 20 CV of wash buffer prior to eluting of the minimal sensor in 2.5 CV elution buffer (50 mM HEPES, pH 7.4, 150 mM NaCl, 1 mM EDTA, 50 mM β-OG, 10 mM maltose). The quality of the purified fusion protein was controlled by SDS-PAGE followed by Instant Blue™ staining (Expedeon) and immunoblotting, respectively. The efficiency of the spin-labeling

was determined in detergent solution for all constructs by double-integration of the respective cwEPR spectra recorded at room temperature and comparison to the signal of a 100 μM MTS standard. The estimated spin-label concentration was related to the protein concentration determined using the OD_{280}. The spin-labeling efficiency ranged between 75% and 95% for all constructs.

Size-Exclusion Chromatography (SEC)
Analytical SEC was used to characterize the oligomeric state of the minimal sensor in detergent solution using a Superdex 200 10/300 increase column in SEC buffer (50 mM HEPES, pH 7.4, 150 mM NaCl, 1 mM EDTA, 50 mM β-OG).

Liposome preparation
All lipids were purchased from Avanti Polar Lipids and stored at $-80°$C as 20 mg/ml stock solutions in chloroform. 1,2-dioleoyl-*sn*-glycero-3-phosphocholine (DOPC), 1-palmitoyl-2-oleoyl-*sn*-glycero-3-phosphocholine (POPC), 1,2-dioleoyl-*sn*-glycero-3-phosphoethanolamine (DOPE), 1-palmitoyl-2-oleoyl-*sn*-glycero-3-phosphoethanolamine (POPE), 1,2-dipalmitoyl-*sn*-glycero-3-phosphocholine (DPPC), L-α-phosphatidylinositol (Soy-PI) and cholesterol were mixed at 60°C to yield the following mixtures: **1)** 50% DOPC, 50% POPC; **2)** 100% POPC; **3)** 90% POPC, 10% DPPC; **4)** 95% POPC, 5% cholesterol; **5)** 90% POPC, 10% cholesterol; **6)** 80% POPC, 10% DPPC, 10% cholesterol; **7)** 80% POPC, 20% cholesterol; **8)** 10% POPC, 40% POPE, 20% soy-PI, 20% DPPC, 10% cholesterol (Figure 5B). Then, the organic solvent was evaporated under a constant stream of nitrogen and the resulting lipid film was dried by application of vacuum for at least 1 hr. For rehydration, the lipid film was mixed with reconstitution buffer (20 mM HEPES, pH 7.4, 150 mM NaCl, 5% glycerol (w/v)) under strong agitation (20 min, 60°C), yielding a lipid concentration of 10 mM. Subsequently, the suspension was incubated in a sonication water bath (50°C) for 30 min prior to snap freezing of the resulting multi-laminar liposomes in liquid N_2.

Reconstitution of the minimal sensor into liposomes
The isolated and spin-labeled minimal sensor was reconstituted into liposomes composed of the lipid compositions 1-8 (described above) at a protein:lipid molar ratio of $\sim$1:400. 160 μl of multi-laminar liposomes (10 mM) were mixed with β-OG for complete solubilization and 0.2 mg of the minimal sensor construct. The final volume was adjusted to 1 ml, resulting in a final concentration of 37 mM β-OG and 0.2 mg/ml of the minimal sensor construct. The mixture was incubated and constantly agitated for 20 min at room temperature. For detergent removal, 100 mg of Bio-Beads^{TM} SM-2 Adsorbent Media (BioRad) were added and the mixture was incubated for 90 min on an overhead rotator. Then, the suspension was transferred to a fresh tube containing 400 mg of SM-2 Bio-Beads^{TM} and again incubated for 90 min. After separation of the SM-2 Bio-Beads^{TM}, proteoliposomes were harvested by centrifugation (90 min, 450,000 x g). The pellet was resuspended in 15 μl reconstitution buffer and snap frozen in liquid N_2 for storage at $-80°$C.

Carbonate extraction with proteoliposomes
A proteoliposome-containing sample was divided into three equal parts and mixed with an equal volume of reconstitution buffer supplemented with either no further additive, with 0.2 M Na_2CO_3 (pH 11.0), or 2% SDS. The resulting samples were incubated on an overhead rotator (30 min, room temperature). Prior to centrifugation (4°C, 90 min, 450,000x g), the Na_2CO_3-treated sample was neutralized by the addition of two volumes of neutralization buffer (200 mM HEPES pH 7.0, 150 mM NaCl), while the volume of the other samples was adjusted by the addition of equivalent amounts of reconstitution buffer. The samples were mixed with 5x reducing sample buffer at a ratio of 2:1 and heated to 95°C for 10 min, for subsequent analysis via SDS-PAGE and Instant Blue^{TM} staining (Expedeon).

Sucrose density gradient centrifugation
A proteoliposome-containing sample was adjusted to a final concentration of 50% (w/v) sucrose to form the bottom layer of a sucrose density step gradient. The proteoliposome-containing bottom layer was overlaid with 3 mL each of the following sucrose solutions in reconstitution buffer: 40% (w/v), 20% (w/v), 10% (w/v) and 0% (w/v). The resulting step-gradient was centrifuged in a SW28.1 rotor (4°C, 100,000x g, 16 hr, no break) and subsequently fractionated in 1 mL fractions. The relative protein and lipid content of the fractions was analyzed by immunoblotting and Hoechst33342 fluorescence spectroscopy.

Hoechst33342 measurements
The fluorescence intensity of the environment-sensitive Hoechst33342 increases significantly in a hydrophobic environment (e.g., liposomes). Thus, Hoechst33342 was used to estimate the relative lipid content of proteoliposome-containing samples. To this end, samples were adjusted to a final concentration of 7 μM Hoechst33342. The suspension was excited at 355 nm (slit width = 3 nm) and an emission spectrum was recorded from 365 nm to 600 nm (slit width = 3 nm) using the Fluoromax-4 spectrometer (Horiba). The lipid content of each sample was estimated by the using the background-corrected fluorescence intensity at 459 nm.

C-Laurdan spectroscopy
Liposome suspensions at a final concentration of 0.33 mM were mixed with C-Laurdan (2p probes) to a final concentration of 0.4 μM, resulting in a 1:832 ratio of C-Laurdan to lipid. The suspension was excited at 375 nm (slit width = 3 nm) and an emission spectrum

was recorded at 30°C from 400 nm to 600 nm (slit width = 3 nm) using a Fluoromax-4 spectrometer (Horiba). The generalized polarization (GP) value was determined as described previously (Covino et al., 2016).

Continuous wave (cw) EPR measurements

Samples with a volume of 15 μl containing the spin-labeled minimal sensor in detergent solution and reconstituted in liposomes, respectively, were filled in glass capillaries with a 1 mm inner diameter (Hirschmann). X-Band cwEPR spectra were recorded using the MiniScope MS 400 EPR spectrometer (Magnetech) with 10 mW microwave power and 0.15 mT field modulation amplitude. EPR spectra were recorded at room temperature for determination of the spin-labeling efficiency and at −115°C for the determination of the inter-spin distances and the polarity of the spin probe's nanoenvironment.

Analysis of cwEPR spectra

Analysis of the cwEPR spectra at low temperature (T = −115°C) provides information on the polarity of the spin probe's nanoenvironment based on the hyperfine splitting Azz and inter-spin distances in a distance range of 1-1.8 nm. In order to derive values for the hyperfine splitting Azz the magnetic field difference between the low and high field peaks was determined resulting in 2Azz. In a semi-quantitative manner, the ratio of the intensities of the low (Lf) and middle field peaks (Mf) (determined as the difference between maximal and minimal intensity divided by two) was used to derive the degree of spectral broadening, representing a measure for inter-spin distances. For plotting, all spectra were intensity normalized using the intensity of the middle field peak.

MD simulations

All molecular configurations were modeled in atomistic details with the CHARMM36 force field (Best et al., 2012; Klauda et al., 2010; Vanommeslaeghe et al., 2010). We initially set up the Ire1-derived sensor peptide (Ire1$^{526–561}$) and the F531R and V535R mutant variants as straight alpha-helices (Pettersen et al., 2004), and with CHARMM-GUI (Jo et al., 2007, 2008, 2009, 2014; Lee et al., 2016; Wu et al., 2014) placed each of them in the center of a pre-equilibrated lipid bilayer, oriented perpendicular to the membrane plane. We considered bilayers of two different compositions matching those of the experiments: composition 1 (50 mol% POPC and 50 mol% DOPC) and composition 7 (80 mol% POPC and 20mol % cholesterol). We placed each bilayer with an inserted peptide in boxes of approximately 14.5x14.5x9 nm^3. We then added explicit TIP3P water and 150 mM sodium chloride. The resulting neutral simulation boxes contain 310 POPC and 310 DOPC molecules (composition 1) and 124 cholesterol and 500 POPC molecules (composition 7) as well as 30,000 water and ion molecules in both cases.

Each structure was relaxed first by minimizing the energy with 5,000 steps of the steepest descent algorithm, and then by careful equilibration in short MD runs at increasing time steps, first in the NVT ensemble by using the Berendsen thermostat (Berendsen et al., 1984) at a temperature of 303 K, then in the NPT ensemble at 1 atm with the semiisotropic Berendsen barostat (Berendsen et al., 1984). MD production simulations were then run with a time step of 2 fs, a velocity rescaling thermostat (Bussi et al., 2007) at 303K, a semiisotropic pressure coupling at 1 atm with the Parrinello-Rahman barostat (Parrinello and Rahman, 1980), and periodic boundary conditions. Electrostatic interactions were evaluated with the Particle-Mesh-Ewald method (Essmann et al., 1995). See Table S3.

Thickness and acyl chain order parameter calculation

We evaluated for each trajectory the two-dimensional thickness and acyl chain order parameter (S$_{CD}$) profiles of the bilayer by using the g_lomepro v1.0.2 tool (Gapsys et al., 2013). We skipped the first 200 ns and sampled frames from the remaining trajectory every 2 ns, dividing the plane of the membrane in 100 × 100 spatial bins.

For each frame the thickness of the bilayer was calculated as the average distance between P atoms in PC lipid headgroups belonging to the same bin in opposite leaflets. The acyl chain order parameter was obtained as the average of the order parameter calculated for each acyl chain atom belonging to the same bin.

Each 2-dimensional profile obtained in this way was aligned with the monomer oriented along the x axis and the N terminus pointing to the positive direction. The alignment was performed by interpolating each thickness and order parameter profile with a 2-dimensional spline of order 3, and rotating it by an appropriate angle around the direction orthogonal to the plane of the membrane. We obtained the required rotation angle by a least-square fit of the C-alpha atoms, restricted to in-plane rigid body rotations, of the helical part of the monomer (residues 528 to 559) in each trajectory to a reference structure properly aligned along the x axis. In order not to lose any data, each frame was extended by considering periodic boundary conditions and cropped to the original dimensions after applying the rotation. The final plots result from a time average of all the aligned 2-dimensional profiles.

MD and analysis software

MD simulations were performed and analyzed with GROMACS 5 (Abraham et al., 2015; Hess et al., 2008; Pronk et al., 2013; Van Der Spoel et al., 2005), NumPy (Van Der Walt et al., 2011), IPython (Pérez and Granger, 2007), Matplotlib (Hunter, 2007) and MDAnalysis (Michaud-Agrawal et al., 2011). Molecular graphics were performed with VMD (Humphrey et al., 1996) and rendered. Videos were encoded with ffmepg and the x264 library.

QUANTIFICATION AND STATISTICAL ANALYSIS

Throughout the manuscript, the data are represented as the average ± SEM. All experiments were performed at least in triplicates. The significance was tested by unpaired Student's t tests. Further information regarding statistical analysis can be found in the figure legends. In the following, for every dataset of this paper the exact value of n is provided:

Figures 1E and 1F: n = 9 (technical triplicates from three individual colonies)
Figure 2A: upper panel n = 3 (three independent experiments)
lower panel n = 3 (three independent experiments)
Figure 2B: left panel WT-: n = 3, WT+: n = 4, V535R+: n = 3
right panel WT-. n = 4, WT+: n = 3, V535R+: n = 3
Figure 2C: left panel WT-: n = 3, WT+: n = 4, V535R+: n = 3
right panel WT-: n = 4, WT+: n = 4, V535R+: n = 3
Figure 3B: left panel n = 9 (technical triplicates from three individual colonies)
right panel n = 3 (from individual colonies)
Figure 3C left panel WT-: n = 3, WT+: n = 4, IF1+: n = 3, IF1/V535R: n = 3
right panel WT-: n = 4, WT+: n = 4, IF1+: n = 3, IF1/V535R: n = 3
Figure 3D left panel WT-: n = 3, WT+: n = 4, IF2+: n = 4, IF2/V535R: n = 3
right panel WT-: n = 4, WT+: n = 4, IF2+: n = 3, IF1/V535R: n = 3
Figure 3E left panel WT-: n = 3, WT+: n = 4, IF2+: n = 4, IF2/V535R: n = 3
right panel WT-: n = 4, WT+: n = 4, IF2+: n = 3, IF1/V535R: n = 3
Figure 3F left panel WT-: n = 3, WT+: n = 4, IF2+: n = 4, IF2/V535R: n = 3
right panel WT-: n = 4, WT+: n = 4, IF2+: n = 3, IF1/V535R: n = 3
Figure 4A left panel WT-: n = 6, WT+: n = 11, ΔIII+: n = 9, ΔIII/V535R: n = 8
right panel WT-: n = 4, WT+: n = 5, ΔIII+: n = 6, ΔIII/V535R: n = 5
Figure 4A left panel WT-: n = 6, WT+: n = 11, ΔIII+: n = 9, ΔIII/V535R: n = 9
right panel WT-: n = 4, WT+: n = 5, ΔIII+: n = 6, ΔIII/V535R: n = 6
Figure 5C from left to right: n = 12, n = 8, n = 4, n = 4, n = 4, n = 4, n = 6, n = 17
Figure 5E from left to right: n = 4, n = 3, n = 3, n = 3, n = 3, n = 3, n = 5, n = 4
Figure 5F from left to right: n = 4, n = 3, n = 3, n = 3, n = 3, n = 3, n = 3, n = 4
Figure S2B n = 3 (from individual clones)
Figure S2G $IRE1_{3xHA-GFP}$: n = 3, $\Delta IRE1$: n = 3, $L13^{543-555}$: n = 9
Figure S2H $IRE1_{3xHA-GFP}$: n = 3, $\Delta IRE1$: n = 3, $L16^{540-555}$: n = 8
Figure S2L $IRE1_{3xHA-GFP}$: n = 3, $\Delta IRE1$: n = 9, R537E: n = 9
Figure S2M $IRE1_{3xHA-GFP}$: n = 6, $\Delta IRE1$: n = 3, ΔIII: n = 6, ΔIII/V535R: n = 6
Figure S4D left panel WT c1: n = 4, c2: n = 3, c7: n = 5, c8: n = 4
left panel F531R c1: n = 4, c2: n = 3, c7: n = 3, c8: n = 4
right panel WT c1: n = 3, c2: n = 3, c7: n = 4, c8: n = 3
right panel F531R c1: n = 3, c2: n = 3, c7: n = 3, c8: n = 3
Figure S4G F531R/R537C closed c1: n = 4, c8: n = 4
F531R/R537C open c1: n = 2, c8: n = 2
R537C closed c1: n = 3, c8: n = 4
R537C open c1: n = 2, c8: n = 2
Figure S6C composition 1 from L534 through I539: n = 3, n = 5, n = 4, n = 4, n = 3, n = 3
composition 8 from L534 through I539: n = 4, n = 5, n = 3, n = 4, n = 3, n = 3
Figure S6D composition 1 from L534 through I539: n = 3, n = 5, n = 4, n = 4, n = 3, n = 3
composition 8 from L534 through I539: n = 4, n = 5, n = 3, n = 4, n = 3, n = 3